



HAL
open science

Alkali pyroxenes and amphiboles: a window on rare earth elements and other high field strength elements behavior through the magmatic-hydrothermal transition of peralkaline granitic systems

Cyrielle Bernard, Guillaume Estrade, Stefano Salvi, Didier Béziat, Martin J Smith

► **To cite this version:**

Cyrielle Bernard, Guillaume Estrade, Stefano Salvi, Didier Béziat, Martin J Smith. Alkali pyroxenes and amphiboles: a window on rare earth elements and other high field strength elements behavior through the magmatic-hydrothermal transition of peralkaline granitic systems. Contributions to Mineralogy and Petrology, 2020, 10.1007/s00410-020-01723-y . hal-02989854

HAL Id: hal-02989854

<https://hal.science/hal-02989854>

Submitted on 5 Nov 2020

HAL is a multi-disciplinary open access archive for the deposit and dissemination of scientific research documents, whether they are published or not. The documents may come from teaching and research institutions in France or abroad, or from public or private research centers.

L'archive ouverte pluridisciplinaire **HAL**, est destinée au dépôt et à la diffusion de documents scientifiques de niveau recherche, publiés ou non, émanant des établissements d'enseignement et de recherche français ou étrangers, des laboratoires publics ou privés.

1 **Alkali pyroxenes and amphiboles: a window on Rare Earth Elements and other High Field Strength**
2 **Elements behavior through the magmatic-hydrothermal transition of peralkaline granitic systems**

3
4 Cyrielle Bernard^a, Guillaume Estrade^{a□}, Stefano Salvi^a, Didier Béziat^a, Martin Smith^b

5 ^a GET, CNRS, UPS, Université de Toulouse III, Toulouse, France

6 ^b School of Environment and Technology, University of Brighton, Brighton, BN2 4GJ, UK

7
8 □ Corresponding author: guillaume.estrade@get.omp.eu

9 ORCID: 0000-0001-6907-7469

10
11
12 **Acknowledgments**

13 This work was supported by an INSU/TelluS grant from CNRS (French National Center for Scientific
14 Research). We thank Anthony Williams-Jones, Olga Vasyukova and Sam Broom-Fendley for providing some of
15 the rock samples from the Strange Lake and Amis complexes and David Chew who helped with LA-ICP-MS
16 mapping. Kathryn Goodenough provided helpful discussion. We also wish to thank CPM reviewers Charles
17 Beard and Adrian Finch for their suggestions and constructive criticisms, which greatly improved the final
18 version of this manuscript.

25

26

27 **Abstract**

28 Peralkaline granites and pegmatites are a prime repository of REE and HFSE, critical raw materials.
29 Although it is accepted that magmatic processes are fundamental in concentrating these metals, the role of
30 hydrothermal fluids in concentrating and fractionating these elements remains unclear. This paper investigates
31 the global reproducibility of the magmatic-hydrothermal evolution of alkaline silica-saturated systems using
32 alkali pyroxene and amphiboles from six alkaline complexes. These minerals contain significant amounts of
33 REE and other HFSE, and pyroxene is stable throughout the magmatic and hydrothermal stages. Amphibole
34 consists of mostly unzoned arfvedsonite, leakeite, and katophorite, while pyroxene is always aegirine. Two types
35 of aegirine were defined. In all complexes, type-I aegirine is zoned; its core is enriched in Ca, REE, Zr, Hf, Sc
36 and Sn, and the rims in Na, Fe³⁺ and contain secondary rare-metal bearing minerals and fluid inclusions. Type-II
37 aegirine replaces amphibole and is oscillatory zoned. We interpret the amphiboles and REE-rich cores of type-I
38 aegirine to have grown during the magmatic stage, whereas the rims of REE-poorer type-I and II aegirine formed
39 during the hydrothermal stage. During magmatic crystallization, REE intake into amphiboles and pyroxene as
40 well as LREE-HREE fractionation were favored by their crystallographic properties and by competition among
41 them and other minerals. During subsequent hydrothermal stages, REE and other HFSE were remobilized,
42 locally reconcentrated and fractionated in mineral pseudomorphs and secondary pyroxene. These observations
43 point out the importance of studying rock-forming minerals such as pyroxenes and amphiboles to unravel
44 geological events controlled by common processes globally.

45

46 **Keywords**

47 Peralkaline granite, pegmatite, pyroxene, amphibole, rare earth elements, high field strength elements

48

49 **Introduction**

50 High Field Strength Elements (HFSE, namely Nb, Ta, Zr, Hf, U, Th, Sn, and Ti), and in particular Rare
51 Earth Elements (REE), are among raw materials considered the most critical today (European Commission
52 2018). They are used in many modern technologies linked to the transition to renewable energy infrastructure

53 (Lucas et al. 2014; Goodenough et al. 2018), but their production is quite restricted, worldwide. REE deposits
54 can be primary (igneous, carbonatites and alkaline systems) or secondary (placers and ion-adsorption)
55 (Chakhmouradian and Wall 2012) and economic concentrations of heavy REE (HREE, Gd to Lu) are rather rare
56 compared to those of light REE (LREE, La to Eu). The latter occur in high amounts mostly in carbonatites and
57 placer deposits and are commonly hosted in fluorcarbonates such as bastnäsite-(Ce), parisite-(Ce) and
58 synchysite-(Ce), and phosphate such as monazite-(Ce). Ion-adsorption deposits provide most of the global HREE
59 production (Chakhmouradian and Wall 2012; U. S. Geological Survey 2019). In alkaline igneous rocks, REE are
60 hosted mainly in monazite-(Ce), xenotime-(Y), fergusonite-(Y), loparite-(Ce) and eudialyte-group minerals
61 (EGM) (Larsen and Sørensen 1987; Chakhmouradian and Wall 2012). Most alkaline igneous rocks are silica-
62 undersaturated, with the silica-saturated variety (i.e., granitic) being quite rare (e.g. Larsen and Sørensen 1987;
63 Ranløv and Dymek 1991; Foland et al. 1993; Kramm and Kogarko 1994; Sheard et al. 2012). However, it is the
64 latter that have high Yb/La ratios compared to other varieties (Fig 1). Pegmatites, which form from the last and
65 most evolved part of silica saturated melts, concentrate the highest amounts of REE and other HFSE.

66 There is a general consensus in the literature that magmatic processes play a role for a pre-enrichment
67 of alkaline rocks in REE and other HFSE (Marks and Markl 2017). These include sourcing from undepleted,
68 more or less metasomatized mantle, crustal contamination, fractional crystallization, and melt-melt immiscibility
69 during magma cooling (Bonin 2007; Nardi and Bitencourt 2009; Chakhmouradian and Zaitsev 2012; Veksler et
70 al. 2012). There is also evidence that hydrothermal processes may play a key role in concentrating these
71 elements to ore grades (e.g. Salvi and Williams-Jones 1990; William-Jones et al. 2012). However, to date, the
72 relative importance of magmatic versus hydrothermal processes is still debated, partly because the processes
73 occurring at the magmatic-hydrothermal transition are hard to document and most studies were carried out in the
74 laboratory (e.g. Migdisov et al. 2016).

75 To fill this gap, it is important to understand the timing of concentration of the REE in natural occurrences.
76 To do so, in this paper we propose for the first time a detailed study of common minerals that carry REE and
77 other HFSE from the magmatic through the hydrothermal stages, from six silica-saturated alkaline occurrences
78 worldwide. The goal is to make out the meaning of textures and link them to the major events that impacted the
79 selected complexes, i.e. the magmatic-hydrothermal transition. Once it is clear which zones of the crystals grew
80 during the magmatic phase and which grew during hydrothermal circulations, we can analyze the REE and other
81 HFSE compositions in the different zones, and infer the timing of concentration and fractionation of the REE.
82 Ideal candidates to do so are the pyroxene and amphibole mineral groups, because of their ubiquitous presence in

83 these rocks and because they have been documented to form during a large span of the evolution of alkaline
84 rocks, from early magmatic to late hydrothermal stages (e.g. Nielsen 1979; Jones and Peckett 1981; Ramløv and
85 Dymek 1991; Marks et al. 2004). In addition, they incorporate a relatively high amount of REE and other HFSE
86 compared to other rock-forming minerals (e.g. alkali feldspar and quartz), even though they are not considered as
87 ore as their partition coefficients for HFSE (except Eu) are not high enough (Fedele et al. 2015). Primary
88 zirconosilicates can also incorporate high levels of HFSE and are common in alkaline rocks, however, they are
89 frequently altered to secondary minerals during the hydrothermal stage. Hence, pyroxenes and amphiboles are
90 the best minerals to evidence the behavior of HFSE throughout the entire process of alkaline granite and
91 pegmatite crystallization.

92

93 **1. Geological background**

94 The six alkaline igneous complexes on which this work focuses are: Ambohimirahavavy (Estrade et al.
95 2014a) and Manongarivo (Donnot 1963) in Madagascar, Amis in Namibia (Schmitt et al. 2002), Evisa in Corsica
96 (Bonin et al. 1978), Khan Bogd in Mongolia (Kovalenko et al. 2006), and Strange Lake in Canada (Currie 1985).
97 These complexes were chosen because all present evidence of hydrothermal circulation and contain high
98 amounts of REE (from 800 ppm in a granite from Khan Bogd to 12 % in a pegmatite from Strange Lake,
99 unpublished data). All complexes contain peralkaline rocks, i.e. their ratio of $(\text{Na}_2\text{O}+\text{K}_2\text{O})/\text{Al}_2\text{O}_3$ is >1 . Some of
100 them have been the subject of in-depth studies, such as the Strange Lake complex which was first studied in the
101 late 1980's (e.g. Miller, 1986; Salvi and Williams-Jones 1990) and still is today (Vasyukova and Williams-Jones
102 2020); others are poorly known, as is the case for the Manongarivo complex, for which the only available
103 information is a mere mention in a French compilation (Donnot, 1963).

104 Although they were emplaced in different geodynamic complexes and at different periods, it appears that the
105 melt source was a metasomatized upper mantle for all six complexes. Crustal contamination and feldspars
106 fractionation, if occurring, are two processes that can enrich alkaline granites in REE. However, the rate of
107 partial melting at the origin of these complexes is still debated, which is an essential parameter given that a lower
108 rate implies a greater accumulation of incompatible elements, REE included, in the newly generated melt. All
109 complexes underwent at least one alteration episode from an orthomagmatic fluid, and some of them an
110 additional late hydrothermal event (identified at Amis, Evisa, and Strange Lake). The composition of the fluids
111 that circulated was measured in fluid inclusions at Ambohimirahavavy and Strange Lake, and inferred from the

112 study of secondary mineral assemblages for the other complexes. The presence of significant amounts of Na⁺
113 and Fe³⁺ in an orthomagmatic fluid is reported for Evisa, the two Malagasy complexes and Strange Lake, and
114 Ca²⁺ was identified at Khan Bogd, Madagascar and Strange Lake. Locally, CO₂ and/or CH₄ were reported at
115 Khan Bogd and Strange Lake, and CO₃²⁻ at Amis. The resulting conclusions are similar for all the complexes:
116 independently of its orthomagmatic or late origin, a F-, Ca-rich fluid is systematically observed and inferred to
117 have mobilized and fractionated the REE. The importance of this process compared to magmatic ones in
118 concentrating and fractionating the REE is still a matter of debate. Comparing six complexes that were emplaced
119 in different geodynamic settings and witnessed different fluid conditions (composition, temperature), is a
120 strategy to highlight common features in order to better constrain and generalize the timing of REE and other
121 HFSE enrichment in alkaline complexes. Below, follows a rapid summary of the main geological features of
122 each complex; more detailed information is provided in Online Resource 1.

123

124 *1.1. Amis complex, Namibia*

125 The Amis complex and the larger Brandberg complex onto which it is juxtaposed are of the same age (132.5
126 to 130.5 My) and are hosted in metasediments of the Damara orogen (~ 550 My; Miller 1983) and volcanic
127 rocks from the Paraná-Etendeka igneous province. Three granite and 4 pegmatite-aplite samples were used for
128 this study. The Amis complex is mainly made of an arfvedsonite granite and aegirine-rich pegmatite-aplites. The
129 Amis complex is highly enriched in REE, other HFSE and volatiles (H₂O, F). Pegmatites and aplites in the
130 north-western part of the Amis complex are particularly enriched in REE mineralizations and uranium. Schmitt
131 et al. (2002) infer that hydrothermal fluids had a very limited impact on the rocks of Amis complex. They affirm
132 that minerals are all mainly magmatic, with the exception of replacement of arfvedsonite by quartz-hematite
133 overgrowths. Based on the study of melt inclusions, they propose that the main process of REE and other HFSE
134 enrichment is magmatic. In contrast, Diehl (1990) proposed that hydrothermal fluids played a significant role,
135 and inferred the replacement of arfvedsonite by aegirine.

136 *1.2. Evisa complex, Corsica*

137

138 The Evisa complex (290 My; Cocherie et al. 2005) was emplaced among metaluminous granitoids. We
139 collected 7 granite and 5 pegmatite samples from the central part of the complex. The complex mainly comprises
140 hypersolvus (perthitic feldspar) and subsolvus (albitic and alkali feldspar) peralkaline granites (Bonin 1990) and

141 associated pegmatites rich in REE-bearing minerals such as monazite-(Ce), apatite, and allanite-(Ce). The
142 hypersolvus granite probably experienced two hydrothermal events: a minor, early episode at the end of
143 crystallization, and a more important second episode, characterized by F-rich fluids, around 200 My (Poitrasson
144 et al. 1998; Bonin et al. 2008). The subsolvus granite is intrusive into the perthitic unit and only experienced the
145 second hydrothermal event, which triggered the replacement of the primary zirconosilicate elpidite by a
146 secondary assemblage (Bonin 1990).

147

148 *1.3. Khan Bogd complex, Mongolia*

149 The Khan Bogd complex is located in the southern Gobi Desert, at the transition between island-arc calc-alkaline
150 differentiated volcanics (329±5 My) and rift-related bimodal basalt–comendite–alkali granite association (318-
151 290 My), and is dated at approximately 290 Ma (Kovalenko et al. 2006). It is among the largest alkaline granite
152 plutons in the world, with a surface area of 1500 km². We collected 3 granite and 7 pegmatite samples, mostly on
153 the western side of the complex. The pluton consists of two ring bodies: a western peralkaline arfvedsonite-
154 bearing granite and a later emplaced, eastern aegirine granite. They are both associated with pegmatites. The
155 pluton has been investigated for mining purposes and estimates indicate grades between 0.3 and 4.5 % REE, the
156 highest grade being located at the top of the granite plutons (estimation of the tonnage is not available,
157 Kovalenko and Yarmolyuk, 1995). The origin of this pluton is linked to a mantle plume and the continental
158 subduction of the South Mongolian Hercynides, but the exact magmatic process is still debated (Kovalenko et al.
159 2006; Kynicky et al. 2011). Kynicky et al. (2011) propose the release of a silica-saturated orthomagmatic fluid
160 that, similarly to Evisa, triggered the replacement of primary elpidite.

161

162 *1.4. Manongarivo and Ambohimirahavy complexes, Madagascar*

163

164 Ambohimirahavy and Manongarivo are the biggest complexes of the Ampasindava province in
165 northwestern Madagascar, yet are not well documented. They were emplaced at circa 24 Ma into marine-shelf
166 carbonates and marine-fluvial siliciclastic sediments of the Isalo Group (Thomas et al. 2009; Cucciniello et al.
167 2016). We collected 3 granite and 4 pegmatite samples from the southern part of the Ambohimirahavy
168 complex. Due to poor outcropping conditions and low occurrence of pegmatites, we could only obtain 3

169 pegmatite samples from Manongarivo. The samples from Ambohimirahavavy were selected according to
170 previous studies from Estrade et al. (2014a, b). Both complexes were likely emplaced in a rifting context and are
171 made of two ring-shaped intrusions side by side, composed of nepheline syenite, alkali feldspar syenite, biotite
172 granite, peralkaline pegmatites, and various volcanic rocks. Due to the recent discovery of rare metals in
173 economic concentrations in ion-adsorption clays, the province drew the attention of a mining exploration
174 company (Estrade et al. 2014b). Granite and pegmatite dykes are the most enriched lithologies in REE and other
175 HFSE. An orthomagmatic fluid metasomatized the complexes in the very last stages of magmatic evolution
176 (Estrade et al. 2014b) and caused the replacement of primary zirconosilicates (eudialyte group minerals (EGM)
177 at Ambohimirahavavy, unknown at Manongarivo) by an assemblage of secondary HFSE-bearing minerals
178 (Lacroix 1923; Rakotovo et al. 2009; Estrade et al. 2018).

179

180 *1.5. Strange Lake complex, Canada*

181 The Strange Lake complex was emplaced 1240 My ago into Paleoproterozoic gneisses and quartz
182 monzonite (Miller 1996) and is considered to represent an extension of the Gardar rift in Greenland (Pillet et al.
183 1989; Boily and Williams-Jones 1994; Siegel et al. 2017a). We chose 3 granite and 4 pegmatite samples which
184 were selected according to previous studies from Salvi and Williams-Jones (1990, 2006; 1995). The Strange
185 Lake complex consists of a hypersolvus granite, while a younger, largely metasomatized transsolvus granite
186 (rare perthite plus two distinct feldspars, previously classified as subsolvus, e.g. Boily and Williams Jones, 1994)
187 surrounds it, forming the majority of the complex (Gysi et al. 2016; Siegel et al. 2017b). These plutons are
188 partially bounded by an outwardly-dipping fracture associated with fluorite and hematite breccia. Two zones of
189 pegmatites have been reported: the Main zone in the center of the complex, and the B zone on the northwestern
190 edge. These magmatic events correlate with a progressive enrichment in REE and other HFSE, from HFSE-poor
191 hypersolvus granite to HFSE-rich transsolvus granite and pegmatites (Miller 1996). Most of the REE are
192 concentrated in the pegmatites. Reserves are estimated at 278 Mt grading 0.93% REE₂O₃ of which 39% are
193 HREE, and 214 Mt at 0.85 % REE₂O₃ in total (Gowans et al. 2017). The complex also contains significant
194 amounts of ZrO₂, Nb₂O₅, and BeO. Two main extensive hydrothermal events affected the complex. The first
195 event is attributed to circulation of a hot (≥ 300 °C) orthomagmatic brine consisting of K- and Na-enriched
196 aqueous and carbonic phases (Salvi and Williams-Jones 2006; Vasyukova and Williams-Jones 2019). The

197 second hydrothermal event consists of a cooler fluid (100 - 200 °C) resulting from mixing of a meteoric fluid
198 and a fluid originating from the granites (Gysi et al. 2016).

199

200

201 **2. Features common to pegmatites and granites from all six complexes**

202 Pegmatites in all complexes are heterogeneous in texture, i.e. they show mineralogical layering visible from
203 the scale of the outcrop to that of a thin section (Fig 3), whereas granites are generally homogeneous. In
204 pegmatites, the layers have grain sizes ranging from a few μm to about 40 cm and locally more (Fig 3).
205 Therefore, to obtain meaningful data, samples for this study were selected from zones of relatively fine grain size
206 (less than a few cm).

207 All pegmatites and granites are dominated by quartz, alkali feldspar (perthites, albite, orthoclase, and/or
208 microcline) that are commonly strongly albitized, plus alkali amphiboles and, mostly in pegmatites, aegirine
209 (Fig 4). Common minerals in both rock types include zircon, pyrochlore group minerals (PGM) and Fe- and Ti-
210 oxides. Other minerals present mostly in pegmatites include Ca and Na zirconosilicates, fluorite, astrophyllite
211 and REE-bearing minerals (typically bastnäsité-(Ce), monazite-(Ce), xenotime-(Y), chevkinite-(Ce), allanite-
212 (Ce), aeschynite-(Y), fergusonite-(Y), britholite-(Y), synchysite-(Ce)). Ti-bearing minerals such as chevkinite-
213 (Ce) and astrophyllite show signs of alteration such as dissolved edges (Fig 4a).

214 Ca and Na zirconosilicates, which are characteristic minerals of apgaitic rocks, are mostly eudialyte-group
215 minerals (EGM) at Ambohimirahavavy (Lacroix 1923; Estrade et al. 2018), and elpidite at Evisa, Khan Bogd
216 and Strange Lake (Bonin 1988; Salvi and Williams-Jones 1990; Grigor'eva et al. 2011). These zirconosilicates
217 were partially to totally replaced by secondary miaskitic mineral assemblages, which commonly form
218 pseudomorphs (Poitrasson et al. 1998; Estrade et al. 2014b; Gysi et al. 2016). The mineralogy of the
219 pseudomorphs varies in the different complexes and consists either of different Zr- and/or REE-bearing minerals
220 (Fig. 4b), or exclusively zircon plus quartz, i.e. typical miaskitic mineral assemblage (Fig 4c). Both
221 pseudomorph types are found in all complexes, except in Amis where our samples only contain the miaskitic
222 zircon-quartz type. Elpidite can also be extensively replaced by other zirconosilicates, namely armstrongite and
223 gittinsite (e.g. Salvi and William-Jones 1995), whereas EGM is only partially replaced by these phases. At Khan
224 Bogd, cathodoluminescence reveals the elpidite is altered from its core, replaced by zircon and armstrongite (Fig
225 4d). Pseudomorphs from Evisa consist of Ca-rich mineral assemblages such as fluorite and parisite-(Ce), the

226 latter growing mostly at the expense of bastnäsite-(Ce). At Manongarivo and Amis, the precursor mineral has not
227 been identified because partial replacement has not been observed in these complexes, so far.

228

229 **3. Analytical methods**

230 Polished thin sections were prepared from all samples from the six complexes and were studied using
231 transmitted light microscopy, cathodoluminescence, Scanning Electron Microscopy (SEM), microprobe, and
232 Laser-Ablation Inductively Coupled Plasma Mass Spectrometry (LA-ICPMS) in order to determine mineral
233 textural relationships and amphiboles and pyroxene zoning.

234 SEM images in back-scattered electron (BSE) mode were collected with a Jeol JSM6360LV SEM coupled
235 with a Bruker silicon drift detector and interpreted with the Esprit software at the Géosciences Environnement
236 Toulouse laboratory, using an accelerating voltage of 20 kV, and a detection time of 40 s.

237 Mineral compositions were determined at the Centre Raymond Castaing in Toulouse, using a CAMECA
238 SX Five electron microprobe (EPMA), with an accelerating voltage of 15 kV, a beam current of 20 nA for
239 pyroxene, 10 nA for amphibole, and a beam diameter of about 2 μm . Quantitative elemental maps were
240 performed on the same instrument, using an accelerating voltage of 15 kV, a beam current of 20 nA and 100 nA
241 for major and minor elements respectively. Counting time was 1 s on each pixel with a step of 0.5 to 4 μm
242 depending on crystal size. Uncertainties were calculated using the method of Ancey et al. (1978). Standards used
243 for calibration as well as detection limits based on repeated measurements are provided in Online Ressource 2.

244 To resolve the oxidation state of iron measured by microprobe, calculations of the valence were made
245 following Droop (1987). In order to verify these measurements, a ^{57}Fe Mössbauer spectrum was collected at the
246 Laboratoire de Chimie de Coordination - University of Toulouse on a constant-acceleration conventional
247 spectrometer, at 80 K and with a 1.85 GBq source of ^{57}Co , over a ± 12 mm/s range with 512 channels. The
248 spectra were acquired via a compact detector c-system and recorded with a Canberra multichannel analyzer,
249 coupled to a computer with Recoil Mossbauer Analysis Software 1.05 from Lagarec and Rancourt (1997).
250 Uncertainties were calculated using the covariance matrix. Pyroxene end-members were then calculated
251 following Mann et al. (2006). Amphiboles end-members were calculated using the spreadsheet available from
252 Locock (2014).

253 Trace element concentrations were determined in situ by LA-ICPMS at the Géosciences Environnement
254 Toulouse laboratory, University of Toulouse, on 30- μm polished thin-sections, using a New Wave Research ESI
255 213 laser coupled to a Thermo-Fisher Element-XR high-resolution ICP-MS. Laser beam diameter varied from 30
256 to 50 μm depending on mineral size, and data were acquired by ablating lines instead of spots in order to prevent
257 intersecting solid inclusion or internal zoning. NIST synthetic glass certified reference materials SRM 610 and
258 SRM 612 were used as external and quality control standards, respectively. Each analysis was normalized using
259 SiO_2 values previously determined by EMPA. The relative precision ranged from 5 to 10% and detection limits,
260 based on repeated measurements, are provided in Online Ressource 3. Trace elements maps were performed at
261 the Trinity College in Dublin according to the method provided in Ubide et al. (2015) using photon machines
262 G2 193 nm UV laser with a Helex two-volume cell coupled to a Thermo iCAPQ ICP-MS. Laser beam spot for
263 maps was 12 μm square, scan speed 8 $\mu\text{m}/\text{s}$ and repetition rate 41 Hz. NIST SRM 610 glass was used as
264 standard. A beam size of 12 μm square typically allows a spatial resolution of 7-10 μm in x and y. This relatively
265 new ablation technique removes only 3-4 μm of material, which allows several maps to be performed on the
266 same area. A first map with all REE and other HFSE was first established, before acquiring a second map with
267 only 5 elements in order to obtain a better signal. LA-ICP-MS maps provide detailed spatial information on
268 zonation in crystals that would not be available otherwise. Analysis were semi-quantitative and compared to
269 microprobe data to obtain the real concentration.

270 To check for the absence of REE mineral inclusions in the pyroxene, we analyzed one sample from the
271 Amis complex by Scanning Transmission Electron Microscopy (STEM) at the Centre Raymond Castaing in
272 Toulouse. Unlike TEM, with STEM the electron beam is focused on a specific point of the sample and scans its
273 surface instead of being focused on the entire surface. This allows a better resolution as well as local chemical
274 identification (e.g. Pennycook and Nellist 2011). The Focused Ion Beam (FIB) was used to prepare the sample
275 for STEM. The FIB is a Hélios 600i operated at 5 kV, and the TEM a JEOL cold-FEG JEM-ARM200F operated
276 at 200 kV equipped with a Cs probe corrector reaching a spatial resolution of 0.078 nm. Images were acquired in
277 high-angle dark field (HAADF) as well as bright field (BF) modes. EDX spectra were recorded on a
278 JEOL CENTURIO SDD detector.

279

280 **4. Amphibole and pyroxene textural and chemical description**

281 *4.1. Textural features*

282 4.1.1. Amphiboles

283 Amphiboles occur in granites and pegmatites as well-developed euhedral crystals (Fig 4e). No significant
284 textural difference was found between amphiboles of the six complexes. They all appear pleochroic, dark green
285 or dark blue to black under plain polarized light (PPL). Their size is highly variable from one complex to another
286 as well as inside pegmatites (typically ranging from 20 μm to 10 cm), but is always comparable with the size of
287 quartz and alkali feldspar crystals in the same rock. Except at Evisa (Fig 4j), amphiboles are not zoned, but they
288 display dissolution/corrosion textures on their rims. They commonly have small quartz and feldspar inclusions,
289 and are in equilibrium with these minerals. Replacement of amphiboles by aegirine and Ti- and/or Fe-oxides is a
290 common feature of peralkaline granitoids (Marks and Markl 2017) and occurs in all pegmatites and some
291 granites (Fig 4e).

292

293 4.1.2. Pyroxene

294 Pyroxene is ubiquitous in pegmatites and granites of all six complexes but present three different
295 textural features. (1) In pegmatites which contain only minor amphibole, it occurs as light to dark green euhedral
296 crystals under PPL ranging from 50 μm to 10 cm. These pyroxene crystals present a core-to-rim zonation
297 pattern, with additional sector zoning in the rims, which are visible under PPL (Fig 4f). Similarly to amphiboles,
298 these crystals are in equilibrium with quartz and alkali feldspar grains. In the rims of this pyroxene, we also
299 found fluid inclusions (Fig 4g) and mineral inclusions that match the composition of those met in pseudomorphs
300 (Fig 4b and h). These pyroxene crystals were found in all studied complexes but Strange Lake. At Khan Bogd,
301 these crystals present an additional zoning area between the core and the sector zoned rims (Fig 4k). (2) In some
302 pegmatites, pyroxene occurs as anhedral crystals of size similar to the one we just described. These crystals are
303 oscillatory zoned, from yellowish to green under PPL (Fig 4i). They commonly include Fe- and/or Ti- oxides.
304 (3) In granites as well as in some pegmatites, anhedral pyroxene is found replacing amphibole (Fig 4e). This
305 pyroxene is also weakly oscillatory zoned. As it replaces amphibole only partially, it's size is smaller than the
306 previously described pyroxene crystals and depends on the original amphibole size. This pyroxene is associated
307 with Fe- and/or Ti- oxides and can sometimes keep the 120° cleavages from the original amphibole.

308 Based on occurrence, size, color, zoning and mineralogical associations, we distinguish two main types of
309 pyroxene in the six complexes we focus on in this study. Type-I matches euhedral zoned pyroxene, and our
310 study focuses mainly on this type. Based on the observation that they present anhedral shape, oscillatory zoning,

311 and are associated with Fe- and/or Ti- oxides, we regroup anhedral single pyroxene crystals and pyroxene
312 replacing amphibole under the denomination type-II.

313

314 4.2. Major element composition

315 4.2.1. Amphiboles

316 Since they present the same textural features, all amphiboles were identified based solely on their
317 chemistry, following the classification of Hawthorne et al. (2012) and in accordance with Leake et al. (1997).
318 The general formula of amphibole is $AB_2C_5T_8O_{22}W_2$ where, in this study, A = Na; B = Na, Ca; C = Fe^{2+} , Fe^{3+} ,
319 Li; T = Ca, Al; and W = OH, F. The rootname is given to these amphiboles based on the composition of the sites
320 A, B and C, and the prefix is added according to the composition of the sites C and W. By strictly following
321 these rules, it appears that some complexes contain only one amphibole type, common to granites and
322 pegmatites, and some contain different amphiboles (Table 1). Ambohimirahavavy (ferro-ferri-fluoro-leakeite;
323 $Na_3Fe_4LiSi_8O_{22}F_2$), Manongarivo and Strange Lake (fluoro-arfvedsonite; $Na_3Fe_5Si_8O_{22}F_2$), and Khan Bogd
324 (arfvedsonite; $Na_3Fe_5Si_8O_{22}(F,OH)_2$) contain only one amphibole. At Amis, amphibole is ferro-ferri-fluoro-
325 leakeite in pegmatites and fluoro-arfvedsonite in the granite. At Evisa, granites and pegmatites contain a zoned
326 amphibole with a core of fluoro-arfvedsonite and a rim of ferro-ferri-fluoro-leakeite (Fig 4L). In addition, the
327 hypersolvus granite from Evisa contains zoned crystals with ferro-ferri-katophorite
328 ($Na_2Ca(Fe^{2+},Mg)_4Fe^{3+}(Si_7Al)O_{22}(OH)_2$) in their core and fluoro-arfvedsonite in their rims (Fig 4j).

329 However, it is important to keep in mind that amphibole is a solid solution, thereby two amphiboles can
330 have different names but be close in composition, and inversely can have the same name but present a
331 compositional range. To avoid these artificial hiatuses and subsets, we focused on the concentration of elements
332 involved, when attributing amphibole names in this study. Hence, the distinction between katophorite and other
333 amphiboles is based on the $Ca/(Ca+Na)$ ratio; being >0.25 (close to 0.4), this makes it a Na-Ca amphibole,
334 compared to values <0.1 for other amphiboles, which are then considered Na-amphiboles. Thereby, ferro-ferri-
335 katophorite at Evisa exhibits a significant compositional gap with the other amphiboles from this study. The
336 distinction between Na-amphiboles is more subtle, and is based on the amount of Li and Fe^{2+}/Fe^{3+} ratio in the C
337 site. Ideally, leakeite has 1 Li apfu; this value is on average 0.6 apfu at Ambohimirahavavy and Evisa, and 0.7
338 apfu at Amis. Arfvedsonites from the other complexes have average Li contents of 0.1-0.3 apfu, validating the
339 distinction proposed here, although these values are intermediate between the two categories. The prefixes ferro-

340 and ferri- refer to the presence of Fe^{2+} and Fe^{3+} , respectively, in the C site. The prefix fluoro- indicates that the F
341 concentration is systematically higher than the concentration of other elements in the W site. In this study, the
342 amounts of F and OH, respectively, are close to 1.1 and 0.9 apfu in arfvedsonite from all complexes but Khan
343 Bogd, where it is closer to 0.9 apfu F and 1.1 apfu OH. Strictly complying with the definition would result in two
344 different names (F and OH varieties), which would vary with each complex. However, this would lead to add
345 unnecessary confusion to the nomenclature, therefore, because the compositional differences are only minor, we
346 chose to ignore this parameter.

347 Within a given category, amphiboles are globally similar in composition in all complexes, including
348 $\text{Fe}^{2+}/\text{Fe}^{3+}$ (around 3 for fluoro-arfvedsonite, 2 for leakeite, and 3.5 for katophorite), with only local variations
349 (Table 1). Chlorine was not detected by microprobe analyses in any of the amphiboles. The main distinction
350 regarding major element composition is found in (fluoro)-arfvedsonite from Manongarivo and Khan Bogd,
351 which both have high contents of Mn (respectively 1.92 and 1.66 % vs 0.50 % in the other complexes, Fig 5d)
352 and $\text{Fe}^{2+}/\text{Fe}^{3+}$ (4.00 and 5.90 vs 2.40). Amphibole from Ambohimirahavavy is also rich in Mn (1.99 %) but does
353 not show a high $\text{Fe}^{2+}/\text{Fe}^{3+}$ value. Fluoro-arfvedsonite from Amis is as rich in F as ferro-ferri-fluoro-leakeite from
354 all other complexes (around 1.6 apfu), which is unusual (Deer et al. 1997b). Amphiboles from pegmatites are
355 generally slightly richer in HFSE, Li and Fe^{3+} than amphiboles from granites.

356

357 4.2.2. Pyroxene

358 Based on composition, pyroxene in granites and pegmatites consists of 85 to 97 % aegirine end-
359 member. Therefore, according to the classification of Morimoto (1988), we will refer to it as aegirine in the
360 following sections of this paper. Pyroxene from Ambohimirahavavy and Khan Bogd is more Ca-rich than the
361 other complexes, but it is still classified as aegirine.

362 Type-I aegirine crystals show a characteristic zoning pattern in pegmatites from all locations: a core-to-
363 rim zoning visible in BSE images (Fig 6n) and a sector zoning visible even by optical microscopy (Fig 6o). This
364 pattern defines 3 main zones, where zone A is the core and zones C and D form sector-zoned rims. Zone C
365 matches the crystallographic sector (110), and zone D sector (100) (Ubide et al. 2019). In a few cases, an
366 additional zone matching the crystallographic sector (010) is also present (e.g. ESM 6). All zones are optically
367 distinguished by different tones of green, attributed to different Ti contents (Fig 6g) (e.g. Strong 1969; Ferguson
368 1973; Nielsen 1979). The contacts between different zoning are sharp in all occurrences (Fig 6). Zone A, the

369 core, is systematically enriched in Ca, Sn, Hf, Zr (Fig 7a, b, c, g) and depleted in Na, Al and Fe³⁺ compared to
370 the other zones (Table 3). In pegmatites, we measured up to 2 wt% ZrO₂ in aegirine cores; although uncommon,
371 Zr-rich aegirine was also described in other localities such as in nepheline syenites from the Motzfeldt Centre,
372 South Greenland (Jones and Peckett 1981; up to 7 wt% ZrO₂) and in metaluminous trachytes from the
373 Warrumbungle Volcano, Australia (Duggan 1988; up to 14.5 wt% ZrO₂). Sector zone C is particularly enriched
374 in Ti and Ca (Fig 6e, g), while D is in Fe (Fig 6c). Two major growth layers are visible in the rims with, in sector
375 C, Ti and Ca decreasing towards the rims of each layer (Fig 6e, g). Al content is low in aegirine from all six
376 complexes (about 0.3 % Al₂O₃ compared to standard average values of 1.2 % reported in aegirine; e.g. Deer et
377 al. 1997a). At Khan Bogd, an additional zone, referred to as zone B, is found between the core and the sector-
378 zoned rims of the crystals (Fig 4k); it shows random oscillations due to variations in many elements, including Ti
379 and Mn. The same zoning pattern, including zone B, was also observed by Ranløv and Dymek (1991) in
380 nepheline syenite from the Narssaq Peninsula. However, they only documented variations in Zr, Ti, Al, Na, Ca
381 and Fe. Larsen (1976) and Piilonen et al. (1998) respectively described a core-to-rim zoning in aegirine from
382 nepheline syenite in the Ilímaussaq and Mont Saint-Hilaire complexes. They report cores enriched in Ca, Fe²⁺,
383 Mg, Mn and Zr compared to rims, which in turn contain higher Al, Ti, Na and Fe³⁺. Shearer and Larsen (1994)
384 supplemented the description of aegirine from Ilímaussaq, by reporting Sr and REE enrichment in cores
385 compared to rims. In our analyses, we did not observe a systematic difference in Mn and Sr contents between
386 core and rims.

387 Type-II aegirine is not sector-zoned but shows oscillatory zoning and we observed a wide variety of
388 compositions depending on which layer was analyzed (Table 2). This zoning is irregular, with no core, made of
389 compositionally varying layers with variable thickness. No common pattern was found among any type-II
390 aegirine crystals, beside their heterogeneity. Many elements are involved, including Fe, Mn, Ca, and Ti (see
391 Online Resource 8). No significant chemical differences were found between type-II aegirine from granites and
392 pegmatites. Type-II aegirine is commonly depleted in Ti and Sn compared to type-I aegirine, except at Khan
393 Bogd. Mg is commonly found in higher concentration in type-II aegirine (Table 2). No significant compositional
394 difference was found between type-II aegirine replacing amphibole in granite and those in pegmatites. At
395 Strange Lake, all observed aegirine crystals are of type-II (Table 2; Salvi and Williams-Jones 1990; Roelofsen
396 1997).

397

398 4.3. Trace element composition

399 4.3.1. Amphiboles

400 Amphiboles from all six complexes have very similar trace element patterns (Table 1). Fluoro-
401 arfvedsonite and ferri-fluoro-leakeite have practically the same composition, with Li contents alone being
402 responsible for the transition from one kind to the other. This cation enters the amphibole structure according to
403 the substitution: ${}^C\text{Li}^+ + {}^C\text{Fe}^{3+} = 2{}^C\text{Fe}^{2+}$, described by Hawthorne et al. (1996). Ferro-ferri-katophorite, which is
404 more calcic than the two other amphiboles, relates to fluoro-arfvedsonite through the substitution: ${}^B\text{Ca}^{2+} + {}^T\text{Al}^{3+}$
405 $= {}^B\text{Na}^+ + {}^T\text{Si}^{4+}$ (Deer et al. 1997b). This last substitution increases the size of the C site, leaving more space to
406 incorporate LREE. Similarly, the coupled substitution $(\text{Mg}, \text{Fe}^{2+}) \rightarrow \text{Fe}^{3+}$ occurring in the C site of amphiboles
407 enhances HREE incorporation (Bottazzi et al. 1999; Siegel et al. 2017b). Amphibole chondrite-normalized REE
408 patterns are systematically enriched in HREE relative to LREE, with a depression in medium REE (MREE, from
409 Eu to Dy). This pattern is unusual compared to more Ca-rich amphibole compositions in which REE patterns are
410 usually enriched in LREE or in MREE (e.g. Marks et al. 2004; Coint et al. 2013). All spectra display a negative
411 Eu anomaly suggesting early plagioclase fractionation (Fig 8). The absolute REE concentrations, though
412 somewhat varying from one complex to another, are quite similar (Fig 8).

413 Despite their similar patterns, the absolute concentrations of REE and other HFSE can vary in
414 amphiboles from one complex to the other. Fluoro-arfvedsonite from Manongarivo and Khan Bogd both have
415 low quantities of Sn (4 and 10 ppm) and HREE (35 and 50 ppm on average). Fluoro-arfvedsonite from
416 Manongarivo also has less LREE than fluoro-arfvedsonite from other complexes (11 vs 60 ppm on average).
417 Ferro-ferri-katophorite from Evisa displays high enrichments in LREE and HREE (respectively 224 and 290
418 ppm) (Fig 8). Ferro-ferri-fluoro-leakeite from Amis is notably different from other complexes in terms of trace
419 elements: it is richer than ferro-ferri-fluoro-leakeite from other complexes in Ti (0.18 vs 0.07 apfu), Sn (360 vs
420 32 ppm), Zn (0.24 vs 0.05 apfu), Pb (97 vs 7 ppm), LREE (168 vs 37 ppm on average) and HREE (140 vs 83
421 ppm on average) (Table 1, Fig 5d). Mn and Zn vary together on a 1:1 relation at Strange Lake, as mentioned in
422 the paper by Hawthorne et al. (2001). Mn and Zn covary in amphiboles from Ambohimirahavavy and Amis as
423 well, but in a different way (respectively 4:1 and 1:3), while at Manongarivo and Khan Bogd they do not appear
424 to be related.

425

426 4.3.2. Pyroxene

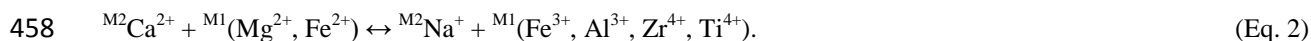
427 Type-I aegirine, similarly to amphiboles, presents comparable trace elements patterns but different
 428 absolute concentrations, from one complex to the other (Table 2). Cores of type-I aegirine from the two
 429 Malagasy complexes have high Zr concentrations compared to other complexes (> 8000 vs 2700 ppm on average
 430 for the other complexes). Khan Bogd aegirine is poorer in Li (17 vs 115 ppm), LREE (12 vs 80 ppm on average)
 431 and HREE (21 vs 125 ppm on average). Type-I aegirine from Amis, similarly to ferro-ferri-fluoro-leakeite in this
 432 complex, shows quite a different trace chemistry than aegirine from other complexes. Average Li is low (50 vs
 433 115 ppm), while other metals are high, e.g. Zn (1780 vs 435 ppm), Sn (3740 vs 700 ppm), Pb (39 vs 7 ppm) and
 434 U (29 vs 0.5 ppm) (Table 2 and Fig 7g). REE and Sc contents in cores of type-I aegirine (zone A) are higher than
 435 in the rims (zones B, C and D) for all complexes (Fig 6, 9 and Table 3; similar maps of aegirine crystals from
 436 each complex are provided in Online Resource 4 to 8). Inside the rims, sector zone C is systematically enriched
 437 in REE compared to sector D (Fig 6k, l, m). Nb and Ta do not have a constant behavior: their contents can be
 438 higher in sector zone C, be present only in fractures, or be enriched in an independent zonation, with all three
 439 cases being possible within the same sample. Similarly to amphiboles, the chondrite-normalized REE patterns of
 440 aegirine show high values for HREE relative to LREE, with lower medium REE. This particular pattern is
 441 known to be specific to Na- and Fe-enriched aegirine (Mahood and Stimac 1990; Shearer and Larsen 1994). The
 442 absolute REE concentrations, are quite similar from one complex to another, although small variations do exist
 443 (Fig 9).

444 Trace element concentrations in type-II aegirine are highly dependent on the zoning pattern. This is
 445 notably true for Sn, Hf and Zr. Compared to type-I aegirine, Sn covaries with Ti instead of Zr. The shape of
 446 type-II aegirine REE patterns is similar to that of type-I, i.e. high HREE relative to LREE, with a depression in
 447 medium REE and a negative Eu anomaly. There is no common pattern in the REE contents of type-II aegirine:
 448 REE contents are higher in type-II than in type-I aegirine at Khan Bogd, generally lower at Evisa, and have
 449 similar values in Madagascar and at Amis (Fig 7g).

450 To verify that the concentrations of REE measured in aegirine truly result from their incorporation in
 451 the crystal structure and not from small mineral inclusions, we used a STEM approach to investigate the core of
 452 a type-I aegirine, where REE are most concentrated. We did not detect any REE mineral inclusion, validating the
 453 premise that the REE are indeed incorporated in the pyroxene's structure. The main substitution involved in this
 454 process is common to type-I aegirine from all pegmatites. The classic aegirine substitution is



456 However, in aegirine from this study there is not enough Fe^{3+} to equilibrate this reaction, hence Al, Zr and Ti,
457 present in aegirine, also contribute to compensate this deficiency, resulting in a new substitution mechanism:



459 However, REE can enter both M1 and M2 sites along with Fe^{3+} and Na^{+} (Beard et al. 2019). In clinopyroxenes,
460 incorporation of REE, as well as other HFSE, is controlled by five crystal-chemistry driven mechanisms, with
461 site parameters being determined by the size of the major elements. The first mechanism is decreasing
462 temperature and increasing melt alkalinity, which usually lowers the REE compatibility. The second mechanism
463 is similar to that for amphiboles and is defined by the substitution $\text{Ca} \rightarrow \text{Na}$, which increases the size of the M2
464 site leaving more space to incorporate LREE. It also decreases the size of the M1 site, making it more adequate
465 to incorporate HREE. The third mechanism takes place in the M1 crystallographic site, where the combined
466 substitution $(\text{Mg}, \text{Fe}^{2+}) \rightarrow \text{Fe}^{3+}$ leads to a charge effects that allows more HREE to enter this site along with Fe^{3+}
467 (Marks et al. 2004; Beard et al. 2019). The fourth mechanism, described by Mollo et al. (2017), is also due to a
468 charge effect. These authors propose the coupled substitution



470 whereby the increase in Al at the expense of Si creates a charge deficiency compensated by the incorporation of
471 REE in the M2 site. In addition, the growth from an environment rich in REE can result in incorporation of high
472 levels of REE in aegirine. Indeed, the adsorption of REE onto aegirine surface during supersaturation may be too
473 fast to equilibrate as crystal growth rate exceeds the internal diffusion rate (Smith et al. 2004).

474 All of the above mechanisms have the potential of favoring the incorporation of REE into pyroxene,
475 however, aegirine in our study having low ${}^{\text{T}}\text{Al}$ and practically no Mg or Fe^{2+} in the M2 site, the mechanism of
476 Mollo et al. is probably not significant in this case. The high REE concentration in aegirine of this study is
477 therefore probably the result of the four other mechanisms that rely on size, charge, and kinetics effect at M sites
478 of aegirine.

479

480 *4.3.3. Ce anomalies*

481 Some amphibole and aegirine chondrite-normalized spectra, mostly from one pegmatite sample from
482 Amis, display a peak in Ce concentration (Fig 8 and 9). The occurrence of this peak being restricted to a few
483 samples, mass interference is excluded. In addition, ICP-MS signals showing peaks during ablation were all

484 excluded so the presence of this Ce peak is not due to mineral inclusions. This peak may be due to the presence
485 of Ce⁴⁺ instead of the usual Ce³⁺. Indeed, Ce⁴⁺ has a smaller ionic radius (0.97 Å) than Ce³⁺ (1.143 Å) for an
486 eight-fold coordination, thereby Ce⁴⁺ substitutes more easily with Fe²⁺ (0.92 Å) and Mg²⁺ (0.89 Å; Shannon
487 1976). The change in oxidation state is commonly interpreted to indicate an increase in oxygen fugacity in the
488 environment that can be either low temperature magmatic (<600 °C, Trail et al. 2012) or hydrothermal (Xu et al.
489 2017).

490

491 **5. Discussion**

492 *5.1. Origin of amphiboles*

493 In the previous sections we have seen that three different amphiboles can be distinguished based on
494 their major and trace chemistry: fluoro-arfvedsonite (Na₃Fe₅Si₈O₂₂(F,OH)₂), ferri-fluoro-leakeite
495 (Na₃Fe₄LiSi₈O₂₂F₂), and ferro-ferri-katophorite (Na₂Ca(Fe²⁺,Mg)₄Fe³⁺(Si₇Al)O₂₂(OH)₂). All of them occur in
496 granites and pegmatites as euhedral crystals and contain inclusions of quartz and feldspar grains (Fig 4e),
497 suggesting co-crystallization. Only amphiboles from Evisa have a variable composition, from fluoro-
498 arfvedsonite or ferro-ferri-katophorite in cores, respectively to ferri-fluoro-leakeite or fluoro-arfvedsonite in the
499 rims. In the other complexes, only one amphibole type is present in granites and in pegmatites. Based on textural
500 observations, we believe these changes are the sign of magmatic evolution. Indeed, the concentration of Li and
501 Na rises in the melt as differentiation occurs, until Li- and Na-rich amphiboles crystallize instead of their Li-
502 poor, Mg-, Ca-rich equivalents. Based on various pieces of evidence, such as having a similar age to that of
503 granite emplacement (Kovalenko et al. 2006), presence of melt inclusions (Schmitt et al. 2002), occurrence as
504 well-developed euhedral crystals, and dissolution/corrosion textures (Estrade et al. 2014a; Gysi et al. 2016), it is
505 accepted in the literature that amphiboles are magmatic phases in peralkaline granites. Hence, in accordance with
506 our observations and those in the literature about the six studied complexes, we conclude that amphiboles of all
507 types in our samples are magmatic. Their variation in trace element composition is directly linked to the
508 environment they grew in, a highly evolved melt, enriched in incompatible elements. Among incompatible
509 elements are the REE, which are known to be preferentially incorporated in alkaline amphiboles along with Na
510 for LREE and Fe³⁺ for HREE (Bottazzi et al. 1999; Siegel et al. 2017b). Due to this crystallo-chemical control,
511 amphiboles can incorporate a lot of REE at the magmatic stage, with a preference for HREE. Slight
512 compositional differences in REE, Zn, Sn, Nb, Zr and Pb between amphiboles of the 6 complexes (Fig 5d) likely

513 reflect parental melt compositions. For example, the presence of ferro-ferri-katophorite in Evisa probably
514 indicates an effect of melt contamination in Ca by the surrounding aluminous granites.

515 As previously described, amphiboles are commonly altered to Fe- and Ti-oxides and to type-II aegirine.
516 Based on textural evidence that at Strange Lake this replacement occurs preferentially along cleavages in altered
517 granites and pegmatites, as well as on mass-balance calculations, Salvi and Williams Jones (1990) identified this
518 pyroxene occurrence as hydrothermal. Because we observed this replacement in all of our samples, it follows
519 that a late hydrothermal event is a common feature in the complexes studied and, by extrapolation, most likely in
520 alkaline rocks in general; indeed, a hydrothermal event was also documented in silica-undersaturated alkaline
521 rocks such as at Ilímaussaq (e.g. [Borst et al., 2016](#)) or at Khibina and Lovozero (e.g. [Arzamastsev et al., 2011](#)).
522 Gysi et al. (2016) and Vasyukova and Williams-Jones (2019) show that at Strange Lake this event is due to a
523 relatively high temperature, Ca-rich fluid. Based on the similarity of amphiboles alteration in all six complexes,
524 we infer that the circulation of an orthomagmatic fluid is a process common to all complexes.

525

526 *5.2. Origin of pyroxene*

527 *5.2.1. Core-to-rim zonation*

528 Even though both types of aegirine identified in all complexes show some kind of zonation, only type-I
529 shows a core-to-rim zonation, with a core enriched in Ca, Zr, Sn, Hf, Sc, REE and depleted in Na, Al and Fe
530 compared to the rims (Fig 6). The rims also have a higher Fe^{3+}/Fe^{2+} ratio than the core. This pattern is
531 systematic for type-I aegirine crystals from all complexes. Type-II aegirine is oscillatory zoned and can replace
532 amphibole.

533 The sharp compositional change between the core and the rims in type-I aegirine (Fig 6) suggests a
534 sudden change in the crystallizing environment. Based on the scarce presence of type-I aegirine where
535 amphiboles are present, we infer that they grew in competition. Only the rims C and D contain fine oscillatory
536 zoning (e.g. TiO_2 on Fig 6g), fluid inclusions (Fig 4g), and, at Ambohimirahavavy, mineral inclusions that match
537 the composition of those measured in hydrothermal pseudomorphs (e.g. zircon, bastnäsite-(Ce), Fig 4b and h).
538 Therefore, we infer that type-I aegirine has a magmatic core (zone A on Fig 6p) while the rims are hydrothermal
539 (zones C and D in Fig 6p). Zone B being only present at Khan Bogd, it will be discussed lower in this section.
540 Chemical zoning in aegirine of our rocks matches that observed by Piilonen et al. (1998) in aegirine from Mont

541 Saint-Hilaire, which they describe as a magmatic pyroxene overgrown by hydrothermal fibrous aegirine. More
542 details about each element in the different zones is provided in the following paragraphs.

543 The variations in Na, Ca, Al, and Fe can be explained by a common process. Type-I aegirine magmatic
544 cores are enriched in Ca, and its hydrothermal rims are richer in Na, Al and Fe³⁺. Evidence such as widespread
545 feldspar albitization, fluid inclusions composition, and the hydrothermal growth of aegirine without amphibole
546 indicate that circulating hydrothermal fluids are oxidizing (above the magnetite-hematite buffer), of relatively
547 high pH and rich in NaCl among other phases (Salvi and Williams-Jones 1996; Smith 2007; Estrade 2014; Gysi
548 et al. 2016). Depletion in Ca and enrichment in Na and Fe while moving on from aegirine magmatic core to
549 hydrothermal rims can then be explained by intake of Na from the hydrothermal fluids and simultaneous
550 crystallization of Ca-rich secondary minerals in the pseudomorphs (fluorite, bastnäsite-(Ce)). This process
551 increases the amount of aegirine endmember compared to hedenbergite endmember which, along with the
552 hydrothermal environment being more oxidizing than the silicate melt, increases the Fe³⁺/Fe²⁺ ratio in the rims.
553 The absolute amount of Al is very low in aegirine of this study, so the observed increase in this element in
554 aegirine rims can be linked only to charge effects, with Al³⁺ being incorporated along with Fe³⁺.

555 Because of their similar behavior, Zr and Hf both occur in the same growth zones. Based on the many
556 arguments in favor of a magmatic core and hydrothermal rims, we propose two hypotheses as to the
557 crystallization timing of type-I aegirine. Jones and Peckett (1981) asserted that formation of Zr-enriched aegirine
558 is enhanced by low oxygen fugacity, and can only occur if no other Zr-bearing phase is growing. Pseudomorphs
559 after primary zirconosilicates were found around aegirine crystals (Fig 4b), hence it is impossible that aegirine
560 grew after the magmatic zirconosilicates. Our first hypothesis is that, in accordance with the observations made
561 by Jones and Peckett (1981), type-I aegirine cores grew before magmatic zirconosilicates, in the magma
562 chamber. In the absence of any mineral Zr has a strong affinity for, Zr partitioned mostly into aegirine. These
563 primary phenocrysts were brought into pegmatites, where primary zirconosilicates began to crystallize,
564 incorporating most of the available Zr. Moving on to the hydrothermal stage, primary zirconosilicates were
565 destabilized and replaced by minerals richer in Zr, including zircon, which form the pseudomorphs. Aegirine
566 rims were then in competition with zircon, which has a high Zr uptake and therefore accounts for the decrease in
567 Zr concentration in aegirine rims. In this hypothesis, aegirine necessarily stopped growing during their migration
568 from the magma chamber to the pegmatites, or it would have resulted in another zonation in the magmatic core.
569 Our second hypothesis is that aegirine core and primary zirconosilicates grew at the same time. In this case the
570 conclusions of Jones and Peckett (1981) do not apply. This may be because their study was based on rocks from

571 the magmatic chamber of Ilímaussaq which had plenty of time to equilibrate during crystallization, whereas our
572 study is based on pegmatites, which crystallize quickly. Anyhow, in this hypothesis the competition between the
573 two minerals resulted in the preference of Zr to go into primary zirconosilicates, but because of the high content
574 of Zr in the melt and its low mobility (Duggan 1988), affinity for aegirine was still high enough to enrich it up to
575 the 2 wt% that we have measured. The subsequent hydrothermal stage is similar to the one in our previous
576 hypothesis, with higher Zr uptake by zircon rather than by zirconosilicates accounting for the decrease in Zr
577 concentration in aegirine rims. A similar behavior was observed for Sn and is most likely due to a similar
578 phenomenon. No Sn-based mineral was found in pseudomorphs, but Sn^{4+} can easily enter in the composition of
579 secondary Ti-oxides because its radius is similar to the Ti^{4+} ion in eight-fold coordination (Shannon 1976). In
580 addition, Sn is known to have a high solubility in Cl-rich fluids (e.g. Keppler and Wyllie 1991), making it easily
581 mobilized. This results in a much higher Sn content in the magmatic zone A than in the rims of aegirine. At
582 Amis, amphibole in pegmatite as well as aegirine are both enriched in Sn, Zn and Pb in comparison with the
583 other complexes of this study (Fig 7g). Ambohimirahavavy and Manongarivo have similar trace elements
584 concentration (Fig 7g) and formed in the same geological context, a few km away from each other. Both
585 amphibole and pyroxene from Khan Bogd have low trace elements concentrations. All these observations tend to
586 indicate that the variations of absolute concentration in REE, Zn, Sn, Zr, U and Pb between aegirine crystals of
587 the 6 complexes (Fig 7g), similarly to amphiboles, likely reflect parent melt compositions.

588

589 5.2.2. *Sector zoning*

590 Sector zoning occurs in the most outer rims in type-I aegirine, involves variations in Ti, Ca, Fe and
591 REE, and was observed in all complexes. Many explanations have been invoked as to the origin of sector zoning,
592 and the latest agree on the fact that it is linked to a crystal growth faster than element diffusion rates (Ubide et al.
593 2019). If this condition is respected, it will result a disequilibrium between the different crystal faces that will not
594 all incorporate the same elements as it normally would (Strong 1969; Ferguson 1973; Larsen 1981). Elements
595 are however incorporated on the different crystal faces in a matter so that charge balance is respected (Ubide et
596 al. 2019). The crystallization rate could also impact the size of protosites (partially formed site on the surface of
597 a growing crystal), which are in equilibrium with the crystallizing environment, and preferentially incorporate
598 elements depending on their charge/radius ratio. If the growth rate is higher than ionic diffusion in the crystal,
599 the protosites will not have enough time to re-equilibrate in size and incorporate different elements on the

600 different faces of the crystal (Nakamura 1973). This higher growth rate is likely related to a lower temperature
601 due to the change from magmatic to hydrothermal environment (Barkov and Martin 2015). However, these
602 considerations must be taken carefully, as most of the research is based on augite and not aegirine.

603 Incorporation of Ti in aegirine is uncommon (Rønsbo et al. 1977; Dyulgerov and Platevoet 2006). Many
604 explanations have been evoked: high temperature, low fO_2 , high fO_2 , low pressure, high activities of TiO_2 and
605 SiO_2 , high activity of alkalis, or a peculiar chemical composition of the environment such as low Zr and Na and
606 high Ca (Ferguson 1973; Flower 1974; Larsen 1976; Rønsbo et al. 1977; Nielsen 1979; Brousse and Raçon
607 1984; Dyulgerov and Platevoet 2006). In our samples, a high temperature is ruled out as Ti incorporation occurs
608 during the hydrothermal stage. As described in the previous section, Zr and Ca concentration are low in the
609 crystallizing environment, and Na is high. Hence, and in accordance with Dyulgerov and Platevoet (2006),
610 Larsen (1976), and Flower (1974), we suggest that in our rocks the incorporation of Ti into hydrothermal
611 aegirine is favored by a high activity of Na and the low availability of Zr. Titanium may have been provided by
612 the alteration of magmatic Ti-bearing minerals, such as astrophyllite (found at Manongarivo, Strange Lake, Khan
613 Bogd and Amis, Fig 4a) chevkinite-(Ce) (found at Ambohimirahavavy, Manongarivo and Evisa), or others such
614 as narsarsukite, låvenite, and aenigmatite.

615

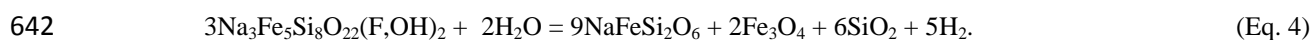
616 5.2.3. *Oscillatory zoning*

617 Oscillatory zoning is present in both types of aegirine. In type-I, it is found in the sector zoned rims C
618 (crystallographic sector (110)) and D (crystallographic sector (100)) as well as in zone B, intermediate between
619 the core and the rims. Considering that zone B in type-I aegirine is only present in our samples in Khan Bogd,
620 and was locally described in aegirine from the South Gardar Province, South Greenland by Ramløv and Dymek
621 (1991), a general process to explain its formation is difficult to establish. Like zones C and D, zone B is poorer
622 in Ca, Zr, Hf, Sn and REE than zone A. It is not specifically enriched in any element, but shows oscillatory
623 zoning in Ti and Mn. We believe that zone B development is related to a specificity in the history of the Khan
624 Bogd complex (Kynicky et al. 2011). In this complex, magmatic zone A aegirine would crystallize before or in
625 competition with primary elpidite. At the hydrothermal stage, primary elpidite altered mostly into a secondary
626 hydrated Ca- and REE-rich elpidite (Fig 4i), and zone B grew simultaneously. The uptake of Ca and Zr by
627 secondary elpidite from the fluid led to the lower concentration of these elements observed in zone B. The final

628 stage, similarly to other complexes, was a more or less extensive pseudomorphism of elpidite and the formation
629 of zones C and D on aegirine.

630 Oscillating concentrations in zones C and D are most likely produced by autocatalytic surface
631 attachment, or boundary layer effect (Ortoleva et al. 1987; London 2008), which occurs when the crystal growth
632 rate exceeds the diffusion rate of components in the fluid. Consider an initial solution saturated in component A,
633 whose adsorption on the crystal surface is fast. As the adsorption progresses, the interface between the crystal
634 and the solution becomes depleted in component A, and switches to saturation in component B. Component B is
635 then adsorbed at the surface of the crystal, until the interface crystal-solution becomes saturated in component A
636 again. This process results in a rhythmic but irregular zoning of aegirine crystals in zones C and D, consistent
637 with a growth in a rapidly changing environment, which is a hydrothermal fluid.

638 Type-II aegirine either replaces amphibole or forms isolated crystals. Both kinds are found associated
639 with Fe- and/or Ti- oxides, and are randomly zoned in many elements (Ti, Ca, Mn, Fe, Hf, Sn, Zr at least). The
640 formation of aegirine from amphibole is known to be hydrothermal (e.g. Salvi and Williams-Jones 1990; Gysi et
641 al. 2016). For arfvedsonite, it follows the reaction provided by Salvi and Williams-Jones (1997):



643 The released Fe generally forms hematite or magnetite. Considering that zoning patterns are the same
644 for all type-II aegirine crystals and that they are systematically found associated with Fe- and/or Ti- oxides, we
645 consider that they all grew replacing amphibole, totally or partially. Hence, we consider type-II aegirine as
646 hydrothermal.

647

648 5.3. REE behavior in amphiboles and aegirine

649 As mentioned in the introduction, amphiboles and pyroxenes, in agreement with their crystal-chemical
650 parameters, can incorporate up to several hundreds of ppm of REE. In addition, their alkaline nature enhances
651 the fractionation of light versus heavy REE through the preferential incorporation of HREE in their structure,
652 resulting in the globally HREE-enriched patterns observed (Fig. 9; Beard et al. 2019). From the amphibole
653 compositions, we know that the melt was rich in F (Table 1). Beard et al. (2020) showed that the more F in the
654 melt, the lower the pyroxene-melt partition coefficient, hence the less REE are incorporated in pyroxene; this
655 affects the LREE more than the HREE and hence contributes to the observed globally HREE-enriched patterns.

656 The REE compositional patterns observed in type-I aegirine are similar to the compositional trends for
657 Zr, Hf and Sn, i.e. they are globally enriched in the core compared to the rims, except for Khan Bogd where the
658 opposite is true (Fig 10, Table 3). Given that the REE concentrations in aegirine at Khan Bogd are very low (2-7
659 ppm for Ce, 4-15 ppm for Y), we believe that this reverse trend is actually not significant (Fig 10). The
660 difference in REE concentration between aegirine zone A and zones B, C and D is due to the competition
661 between aegirine and zirconosilicates for these elements, during the magmatic stage for zone A, and during the
662 hydrothermal stage for the zones B, C and D. Scandium is sometimes grouped with REE, hence, it is not
663 surprising to observe that, similarly to REE, it is enriched in the core of type-I aegirine.

664 During the hydrothermal stage, aegirine is in competition with an altered, REE-enriched elpidite for
665 zone B, and with REE-bearing minerals in pseudomorphs (e.g. bastnäsite-(Ce)) for zones C - (110) and D -
666 (100). We therefore suggest that it is a competition for REE between aegirine and coprecipitating minerals
667 having each a different REE affinity which explains the variations in REE concentrations among the aegirine
668 core-to-rim zones. REE are also affected by sector zoning and are more concentrated in zone C than D, along
669 with Ti and Ca. Beard et al. (2019) studied experimentally the fractionation of REE in clinopyroxene in
670 peralkaline melts and showed that the more Na and less Ca in M2 site of pyroxene, the smaller the M1 site, and
671 the more HREE are incorporated. In addition, the authors mention that physico-chemical parameters not
672 recorded in the composition of clinopyroxene, such as pressure, also play a significant role in the size of the M1
673 site. However, this mechanism is well defined only for pyroxenes whose aegirine component is not higher than
674 50 %. In our samples, the substitution $\text{Ca} \rightarrow \text{Na}$ simply cannot be responsible for the zonation observed, as more
675 REE are found in the C sector, where Ca concentration is also higher. In addition, in Ca-rich pyroxenes such as
676 diopside and augite, Ca was not reported to fractionate between sectors (e.g. [Ubide et al., 2019](#)), which is another
677 argument for the occurrence of a different exchange mechanism in our samples.

678 In addition to the above variations in bulk abundance, cores and rims also preferentially incorporate
679 REE with lower or higher atomic numbers, creating a fractionation between the heavy and light REE. To
680 evaluate this process, we calculated the percentages of REE enrichment or depletion from core to rim in type-I
681 pyroxene. To do so, data obtained by LA-ICPMS were assigned either to the core or to the rim, based on their Zr
682 content and zoning SEM observations. By comparing these two parameters, we were able to determine a
683 threshold value, unique to each complex, below which a given aegirine analysis should be considered as rim, and
684 above which core. These data were averaged out to obtain a single value each for core and rim (Fig 10). Finally,
685 we calculated the extent of loss or enrichment between core and rim for each REE, according to:

686 $d = \frac{C-R}{C} \times 100$ (Eq. 5)

687 where d represents the percentage difference between core and rim, C and R the mean values obtained for core
 688 and rim, respectively. Error bars shown in Fig 11 were obtained using common error calculation formulae,
 689 namely (Eq. 6) for the mean and (Eq. 7) for the percentage.

690 $\overline{err} = \sqrt{\frac{\sum_{x=1}^n (err_x)^2}{n}}$ (Eq. 6)

691 $d_{err} = \frac{C-R}{C} \sqrt{\frac{err_C^2 - err_R^2}{(C-R)^2} + \frac{err_C^2}{C^2}}$ (Eq. 7)

692 with \overline{err} being the mean error, n the number of measurements, d_{err} the error on the percentage variation from
 693 core to rim, err_C the mean error on core data, and err_R the mean error on rim data. Resulting values indicate an
 694 enrichment in that element in the rim compared to the core when positive, while negative ones indicate a
 695 depletion (Fig 11).

696 From the calculation of the percentage of depletion of REE from core to rim (Fig 11) we see that Amis,
 697 Manongarivo and Evisa have a trend with a more important depletion of LREE than HREE: from 40-80 % to 20-
 698 40 % depletion, respectively. Ambohimirahavy shows the opposite trend: around 30 % of LREE depletion for
 699 45% of HREE depletion. The latter trend is not as obvious as for other complexes, but it is still significant.

700

701 *5.4. General model*

702 We propose a global model of formation for amphiboles and aegirine in pegmatites (Fig 12). During the
 703 magmatic stage, two hypotheses remain. In the first one, amphibole and zone A of type-I aegirine grew at early
 704 magmatic stage, concentrating Zr and REE. In the second hypothesis, type-I aegirine core, amphibole and
 705 zirconosilicates grew in competition. Most Zr was incorporated in the zirconosilicates, as well as REE if the
 706 primary zirconosilicates was EGM. However, highly differentiated alkaline melts being particularly enriched in
 707 Zr and REE, there is an extra supply in these metals which, combined with a fast crystallization, could be
 708 incorporated by the structures of amphiboles and aegirine (Fig 12a).

709 During the orthomagmatic hydrothermal stage, amphiboles did not grow anymore, and type-I aegirine
 710 was in competition with secondary Zr- and REE-bearing minerals (generally zircon and bastnäsite-(Ce)) that
 711 formed pseudomorphs after primary zirconosilicates. Since HFSE have much higher affinity for these secondary

712 minerals, their concentrations globally decreased in the co-crystallizing aegirine rims. It is also during this stage
713 that type-II aegirine crystals nucleated. Nevertheless, competition does not explain the observed LREE-HREE
714 fractionation. Residual melt, depleted in incompatible elements, likely crystallized late quartz and feldspar.

715 Given the overwhelming evidence for circulation of an orthomagmatic fluid in all complexes, we propose
716 that fractionation results from variations in fluid composition. From the presence of secondary minerals such as
717 bastnäsite-(Ce) and fluorite, and the study of fluid inclusions at Ambohimirahavavy and Strange Lake (Estrade
718 2014; Vasyukova et al. 2016), we know that the fluids contained at least the anions Cl^- , F^- , and CO_3^{2-} . These
719 species have the ability to form stable complexes with the REE, to different extents. F^- and CO_3^{2-} together are
720 mostly depositional ligands (Migdisov et al. 2016), thus precipitate with REE typically forming the LREE-
721 bearing bastnäsite-(Ce). On the other hand, Cl^- is a weak but abundant ligand that can transport LREE more
722 easily than the heavy ones (Migdisov et al. 2016). If present as a transporting ligand, F^- also transports more
723 LREE than HREE (Beard et al. 2020). We can thus infer that, depending on the relative concentrations of each
724 ligand, fractionation of light vs heavy REE would be specific to each complex (Fig 12b). As long as fluid flow
725 continued, aegirine rims kept growing, although REE incorporation and LREE-HREE fractionation kept
726 diminishing. By the time the hydrothermal stage waned, the two aegirine types were in equilibrium with the
727 pseudomorphs and the partially replaced amphiboles (Fig 12c).

728

729 6. Conclusions

730

731 By comparing amphibole and pyroxene in six alkaline complexes worldwide, our study highlights that
732 despite different geodynamic contexts, mineralogy, and REE enrichment, there is a general crystallization
733 process common to all studied alkaline pegmatites. We believe this process can be generalized to all alkaline
734 SiO_2 -saturated pegmatites worldwide, with local variations in mineralogy and REE-enrichment and fractionation
735 rates. This crystallization process includes at least two main stages, respectively magmatic and hydrothermal.

736 From the study of the composition of amphibole and type-I aegirine core, we document the magmatic stage,
737 during which a systematic primary enrichment in REE, HFSE and a LREE-HREE fractionation occurs. This
738 enrichment is common to all complexes and linked to the properties of the extremely differentiated alkaline
739 magma. The enrichment rate, however, differs from one complex to another. The REE fractionation is most

740 likely due to crystallographic properties of aegirine and alkali amphiboles that preferentially incorporate HREE
741 and do not represent an inherent property of the melt.

742 From the study of the texture and composition of type-I aegirine rims and type-II aegirine, we document
743 similarities between complexes during the hydrothermal stage, at which amphiboles stop growing, type-I
744 aegirine grows sector-zoned rims, and type-II aegirine begins replacing amphibole along with Fe- and Ti-oxides.
745 The drop in REE concentration in hydrothermal aegirine of all complexes shows that REE hydrothermal
746 enrichment is globally less effective than magmatic REE enrichment, but still effective. The observed REE
747 fractionation in all complexes show that hydrothermal fluids also have the ability to fractionate LREE-HREE
748 through their transportation associated with ligands such as F⁻, Cl⁻. The rate of fractionation as well as the
749 amount of mobilized REE depends on the local properties of the circulating fluid(s). These observations show
750 that hydrothermal flow is mandatory in order to enhance the concentration of the REE, and specially HREE, in
751 alkaline pegmatites to ore levels.

752

753 **References**

- 754 Ancey M, Bastenaire F, Tixier R (1978) Application des méthodes statistiques en microanalyse. *Microanal*
755 *Microsc Électronique À Balayage* 323:11–16
- 756 Arzamastsev AA, Arzamastseva LV, Zارايسкий GP (2011) Contact interaction of agpaitic magmas with basement
757 gneisses: an example of the Khibina and Lovozero massifs. *Petrology* 19:109–133
- 758 Barkov AY, Martin RF (2015) Anomalous Cr-rich zones in sector-zoned clinopyroxene macrocrysts in gabbro,
759 Mont Royal, Montreal, Quebec, Canada. *Can Mineral* 53:895–910
- 760 Beard C, van Hinsberg V, Stix J, Wilke M (2020) The effect of fluorine on clinopyroxene / melt trace-element
761 partitioning. *Contrib Mineral Petrol*. <https://doi.org/doi: 10.1007/s00410-020-1672-5>
- 762 Beard CD, van Hinsberg VJ, Stix J, Wilke M (2019) Clinopyroxene/melt trace element partitioning in sodic
763 alkaline magmas. *J Petrol*. <https://doi.org/10.1093/petrology/egz052>
- 764 Boily M, Williams-Jones AE (1994) The role of magmatic and hydrothermal processes in the chemical evolution
765 of the Strange Lake plutonic complex, Quebec-Labrador. *Contrib Mineral Petrol* 118:33–47
- 766 Bonin B (1988) Peralkaline granites in Corsica: some petrological and geochemical constraints. *Rendiconti Della*
767 *Soc Ital Mineral E Petrol* 73:1191–1194
- 768 Bonin B (2007) A-type granites and related rocks: evolution of a concept, problems and prospects. *Lithos* 97:1–
769 29
- 770 Bonin B (1990) Les granites des complexes annulaires, BRGM. Office des publications universitaires
- 771 Bonin B, Grelou-Orsini C, Vialette Y (1978) Age, origin and evolution of the anorogenic complex of Evisa
772 (Corsica): A K-Li-Rb-Sr study. *Contrib Mineral Petrol* 65:425–432

- 773 Bonin B, Platevoet B, Poitrasson F, Renna MR (2008) Eurogranites-IGCP510 2008 Joint Field-meeting—
774 Alkaline The Permian–Triassic A-type Volcanic–Plutonic Igneous Suite of Corsica. In: 33th
775 International Geological Congress in Oslo, Norway Convention Centre, Lillestrom, Norway
- 776 Borst AM, Friis H, Andersen T, et al (2016) Zirconosilicates in the kakortokites of the Ilímaussaq complex,
777 South Greenland: Implications for fluid evolution and high-field-strength and rare-earth element
778 mineralization in agpaite systems. *Mineral Mag* 80:5–30
- 779 Bottazzi P, Tiepolo M, Vannucci R, et al (1999) Distinct site preferences for heavy and light REE in amphibole
780 and the prediction of Amph/L D REE. *Contrib Mineral Petrol* 137:36–45
- 781 Brousse R, Rançon JP (1984) Crystallization trends of pyroxenes from agpaite phonolites (Cantal, France).
782 *Mineral Mag* 48:39–45
- 783 Chakhmouradian AR, Wall F (2012) Rare earth elements: minerals, mines, magnets (and more). *Elements*
784 8:333–340
- 785 Chakhmouradian AR, Zaitsev AN (2012) Rare earth mineralization in igneous rocks: sources and processes.
786 *Elements* 8:347–353
- 787 Chengyu W, Dianhao H, Zhongxun G (1990) REE Geochemistry in the Weathered Crust of Granites, Longnan
788 Area, Jiangxi Province. *Acta Geol Sin - Engl Ed* 3:193–209. [https://doi.org/10.1111/j.1755-
789 6724.1990.mp3002006.x](https://doi.org/10.1111/j.1755-6724.1990.mp3002006.x)
- 790 Cocherie A, Rossi P, Fanning CM, Guerrot C (2005) Comparative use of TIMS and SHRIMP for U–Pb zircon
791 dating of A-type granites and mafic tholeiitic layered complexes and dykes from the Corsican Batholith
792 (France). *Lithos* 82:185–219
- 793 Coint N, Barnes CG, Yoshinobu AS, et al (2013) Use of trace element abundances in augite and hornblende to
794 determine the size, connectivity, timing, and evolution of magma batches in a tilted batholith.
795 *Geosphere* 9:1747–1765
- 796 Cucciniello C, Tucker RD, Jourdan F, et al (2016) The age and petrogenesis of alkaline magmatism in the
797 Ampasindava Peninsula and Nosy Be archipelago, northern Madagascar | SpringerLink. *Mineral Petrol*
798 110:309–331. <https://doi.org/10.1007/s00710-015-0387-1>
- 799 Currie KL (1985) An unusual peralkaline granite near lac Brisson, Quebec-Labrador. *Curr Res* 73–80
- 800 Deer WA, Howie RA, Zussman J (1997a) *Rock-Forming Minerals: Single-chain Silicates, Volume 2A.*
801 Geological Society of London
- 802 Deer WA, Howie RA, Zussman J (1997b) *Rock-forming Minerals: Double-Chain Silicates, Volume 2B.*
803 Geological Society of London
- 804 Diehl M (1990) Geology, mineralogy, geochemistry and hydrothermal alteration of the Brandberg alkaline
805 complex, Namibia. Geological Survey of Namibia
- 806 Donnot M (1963) Côte Nord-Ouest du complexe intrusif alcalin; Ampasindava-Manongarivo
- 807 Droop GTR (1987) A general equation for estimating Fe³⁺ concentrations in ferromagnesian silicates and
808 oxides from microprobe analyses, using stoichiometric criteria. *Mineral Mag* 51:431–435
- 809 Duggan MB (1988) Zirconium-rich sodic pyroxenes in felsic volcanics from the Warrumbungle Volcano,
810 Central New South Wales, Australia. *Mineral Mag* 52:491–496
- 811 Dyulgerov MM, Platevoet B (2006) Unusual Ti and Zr aegirine-augite and potassic magnesio-arfvedsonite in the
812 peralkaline potassic oversaturated Buhovo-Seslavtzi complex, Bulgaria. *Eur J Mineral* 18:127–138
- 813 Estrade G (2014) Le complexe cénozoïque alcalin d’Ambohimirahavavy à Madagascar : origine, évolution et
814 minéralisations en métaux rares. Toulouse 3

- 815 Estrade G, Béziat D, Salvi S, et al (2014a) Unusual evolution of silica-under-and-oversaturated alkaline rocks in
816 the Cenozoic Ambohimirahavavy Complex (Madagascar): Mineralogical and geochemical evidence.
817 *Lithos* 206:361–383
- 818 Estrade G, Salvi S, Béziat D, et al (2014b) REE and HFSE mineralization in peralkaline granites of the
819 Ambohimirahavavy alkaline complex, Ampasindava peninsula, Madagascar. *J Afr Earth Sci* 94:141–
820 155
- 821 Estrade G, Salvi S, Béziat D (2018) Crystallization and destabilization of eudialyte-group minerals in peralkaline
822 granite and pegmatite: a case study from the Ambohimirahavavy complex, Madagascar. *Mineral Mag*
823 82:375–399. <https://doi.org/10.1180/minmag.2017.081.053>
- 824 European Commission (2018) Report on Critical Raw Materials and the Circular Economy.
825 <http://ec.europa.eu/docsroom/documents/27348>. Accessed 25 Apr 2018
- 826 Fedele L, Lustrino M, Melluso L, et al (2015) Trace-element partitioning between plagioclase, alkali feldspar,
827 Ti-magnetite, biotite, apatite, and evolved potassic liquids from Campi Flegrei (Southern Italy). *Am*
828 *Mineral* 100:233–249
- 829 Ferguson AK (1973) On hour-glass sector zoning in clinopyroxene. *Mineral Mag* 39:321–325.
830 <https://doi.org/10.1180/minmag.1973.039.303.08>
- 831 Flower MF (1974) Phase relations of titan-acmite in the system Na₂O-Fe₂O₃-Al₂O₃-TiO₂-SiO₂ at 1000 bars
832 total water pressure. *Am Mineral J Earth Planet Mater* 59:536–548
- 833 Foland KA, Landoll JD, Henderson CMB, Chen J (1993) Formation of cogenetic quartz and nepheline syenites.
834 *Geochim Cosmochim Acta* 57:697–704. [https://doi.org/10.1016/0016-7037\(93\)90380-F](https://doi.org/10.1016/0016-7037(93)90380-F)
- 835 Goodenough KM, Wall F, Merriman D (2018) The Rare Earth Elements: Demand, Global Resources, and
836 Challenges for Resourcing Future Generations. *Nat Resour Res* 27:201–216.
837 <https://doi.org/10.1007/s11053-017-9336-5>
- 838 Gowans RM, Lewis WJ, Zalnieriunas RV (2017) Quest Rare Minerals Ltd.: Strange Lake Resource Estimation
- 839 Grigor'eva AA, Zubkova NV, Pekov IV, et al (2011) Crystal chemistry of elpidite from Khan Bogdo (Mongolia)
840 and its K-and Rb-exchanged forms. *Crystallogr Rep* 56:832
- 841 Gysi AP, Williams-Jones AE, Collins P (2016) Lithogeochemical vectors for hydrothermal processes in the
842 Strange Lake peralkaline granitic REE-Zr-Nb deposit. *Econ Geol* 111:1241–1276
- 843 Hatch GP (2015) TMR Advanced Rare-Earth Projects Index — Technology Metals Research.
844 <http://www.techmetalsresearch.com/metrics-indices/tmr-advanced-rare-earth-projects-index/>. Accessed
845 27 Jun 2018
- 846 Hawthorne FC, Oberti R, Cannillo E, et al (2001) Li-bearing arfvedsonitic amphiboles from the Strange Lake
847 peralkaline granite, Quebec. *Can Mineral* 39:1161–1170
- 848 Hawthorne FC, Oberti R, Harlow GE, et al (2012) Nomenclature of the amphibole supergroup. *Am Mineral*
849 97:2031–2048
- 850 Hawthorne FC, Oberti R, Ungaretti L, et al (1996) Fluor-ferro-leakeite, NaNa₂ (Fe₂+ 2Fe₃+ 2Li) Si₈O₂₂F₂, a
851 new alkali amphibole from the Canada Pinabete pluton, Questa, New Mexico, USA. *Am Mineral*
852 81:226–228
- 853 Ishihara S, Hua R, Hoshino M, Murakami H (2008) REE abundance and REE minerals in granitic rocks in the
854 Nanling range, Jiangxi Province, southern China, and generation of the REE-rich weathered crust
855 deposits. *Resour Geol* 58:355–372
- 856 Jones AP, Peckett A (1981) Zirconium-bearing aegirines from Motzfeldt, south Greenland. *Contrib Mineral*
857 *Petrol* 75:251–255

- 858 Keppler H, Wyllie PJ (1991) Partitioning of Cu, Sn, Mo, W, U, and Th between melt and aqueous fluid in the
859 systems haplogranite-H₂O-HCl and haplogranite-H₂O-HF. *Contrib Mineral Petrol* 109:139–150
- 860 Kogarko LN, Williams CT, Woolley AR (2002) Chemical evolution and petrogenetic implications of loparite in
861 the layered, agpaitic Lovozero complex, Kola Peninsula, Russia. *Mineral Petrol* 74:1–24
- 862 Kovalenko VI, Yarmolyuk VV, Sal'nikova EB, et al (2006) Geology, geochronology, and geodynamics of the
863 Khan Bogd alkali granite pluton in southern Mongolia. *Geotectonics* 40:450–466
- 864 Kovalenko VI, Yarmolyuk VV (1995) Endogenous rare metal ore formations and rare metal metallogeny of
865 Mongolia. *Econ Geol* 90:520–529
- 866 Kramm U, Kogarko LN (1994) Nd and Sr isotope signatures of the Khibina and Lovozero agpaitic centres, Kola
867 Alkaline province, Russia. *Lithos* 32:225–242. [https://doi.org/10.1016/0024-4937\(94\)90041-8](https://doi.org/10.1016/0024-4937(94)90041-8)
- 868 Kynicky J, Chakhmouradian AR, Xu C, et al (2011) Distribution and evolution of zirconium mineralization in
869 peralkaline granites and associated pegmatites of the Khan Bogd complex, southern Mongolia. *Can*
870 *Mineral* 49:947–965
- 871 Lacroix A (1923) *Minéralogie de Madagascar*. A. Challamel, éditeur, Librairie maritime et coloniale
- 872 Lagarec K, Rancourt DG (1997) Extended Voigt-based analytic lineshape method for determining N-
873 dimensional correlated hyperfine parameter distributions in Mössbauer spectroscopy. *Nucl Instrum*
874 *Methods Phys Res Sect B Beam Interact Mater At* 129:266–280
- 875 Larsen LM (1976) Clinopyroxenes and coexisting mafic minerals from the alkaline Ilímaussaq intrusion, South
876 Greenland. *J Petrol* 17:258–290
- 877 Larsen LM (1981) Sector zoned aegirine from the Ilímaussaq alkaline intrusion, South Greenland. *Contrib*
878 *Mineral Petrol* 76:285–291
- 879 Larsen LM, Sørensen H (1987) The Ilímaussaq intrusion—progressive crystallization and formation of layering
880 in an agpaitic magma. *Geol Soc Lond Spec Publ* 30:473–488
- 881 Leake BE, Woolley AR, Arps CE, et al (1997) Nomenclature of amphiboles; report of the Subcommittee on
882 Amphiboles of the International Mineralogical Association Commission on new minerals and mineral
883 names. *Mineral Mag* 61:295–310
- 884 Li X-H, Li W-X, Li Q-L, et al (2010) Petrogenesis and tectonic significance of the 850 Ma Gangbian alkaline
885 complex in South China: evidence from in situ zircon U–Pb dating, Hf–O isotopes and whole-rock
886 geochemistry. *Lithos* 114:1–15
- 887 Liu Y, Chen Z, Yang Z, et al (2015) Mineralogical and geochemical studies of brecciated ores in the Dalucao
888 REE deposit, Sichuan Province, southwestern China. *Ore Geol Rev* 70:613–636.
889 <https://doi.org/10.1016/j.oregeorev.2015.03.006>
- 890 Locock AJ (2014) An Excel spreadsheet to classify chemical analyses of amphiboles following the IMA 2012
891 recommendations. *Comput Geosci* 62:1–11
- 892 London D (2008) Pegmatites. *Sp. Pub. 10. Can Miner* 347:
- 893 Lucas J, Lucas P, Le Mercier T, et al (2014) Rare earths: science, technology, production and use. Elsevier
- 894 Mahood GA, Stimac JA (1990) Trace-element partitioning in pantellerites and trachytes. *Geochim Cosmochim*
895 *Acta* 54:2257–2276. [https://doi.org/10.1016/0016-7037\(90\)90050-U](https://doi.org/10.1016/0016-7037(90)90050-U)
- 896 Mann U, Marks M, Markl G (2006) Influence of oxygen fugacity on mineral compositions in peralkaline melts:
897 The Katzenbuckel volcano, Southwest Germany. *Lithos* 91:262–285.
898 <https://doi.org/10.1016/j.lithos.2005.09.004>

- 899 Marks M, Halama R, Wenzel T, Markl G (2004) Trace element variations in clinopyroxene and amphibole from
900 alkaline to peralkaline syenites and granites: implications for mineral–melt trace-element partitioning.
901 *Chem Geol* 211:185–215
- 902 Marks MA, Markl G (2017) A global review on agpaitic rocks. *Earth-Sci Rev* 173:229–258
- 903 Migdisov A, Williams-Jones AE, Brugger J, Caporuscio FA (2016) Hydrothermal transport, deposition, and
904 fractionation of the REE: Experimental data and thermodynamic calculations. *Chem Geol* 439:13–42
- 905 Miller RM (1983) The Pan-African Damara Orogen of South West Africa/Namibia. *Evol Damara Orogen South*
906 *West Afr*
- 907 Miller RR (1996) Structural and textural evolution of the Strange Lake peralkaline rare-element (NYF) granitic
908 pegmatite, Quebec-Labrador. *Can Mineral* 34:349–371
- 909 Mollo S, Blundy JD, Giacomoni P, et al (2017) Clinopyroxene-melt element partitioning during interaction
910 between trachybasaltic magma and siliceous crust: Clues from quartzite enclaves at Mt. Etna volcano.
911 *Lithos* 284–285:447–461. <https://doi.org/10.1016/j.lithos.2017.05.003>
- 912 Moore M, Chakhmouradian AR, Mariano AN, Sidhu R (2015) Evolution of rare-earth mineralization in the Bear
913 Lodge carbonatite, Wyoming: Mineralogical and isotopic evidence. *Ore Geol Rev* 64:499–521.
914 <https://doi.org/10.1016/j.oregeorev.2014.03.015>
- 915 Morimoto N (1988) Nomenclature of Pyroxenes. *Mineral Petrol* 39:55–76
- 916 Nakamura Y (1973) Origin of sector-zoning of igneous clinopyroxenes. *Am Mineral* 58:986–990
- 917 Nardi LVS, Bitencourt M de F (2009) A-type granitic rocks in post-collisional settings in southernmost Brazil:
918 their classification and relationship with tectonics and magmatic series. *Can Mineral* 47:1493–1503.
919 <https://doi.org/10.3749/canmin.47.6.1493>
- 920 Nielsen TFD (1979) The occurrence and formation of Ti-aegirines in peralkaline syenites. *Contrib Mineral*
921 *Petrol* 69:235–244
- 922 Ortoleva P, Merino E, Moore C, Chadam J (1987) Geochemical self-organization I; reaction-transport feedbacks
923 and modeling approach. *Am J Sci* 287:979–1007
- 924 Pennycook SJ, Nellist PD (2011) *Scanning Transmission Electron Microscopy: Imaging and Analysis*. Springer
925 Science & Business Media
- 926 Piilonen PC, McDonald AM, Lalonde AE (1998) The crystal chemistry of aegirine from Mont Saint-Hilaire,
927 Quebec. *Can Mineral* 36:779–791
- 928 Pillet D, Bonhomme MG, Duthou JL, Chenevoy M (1989) Chronologie Rb/Sr et K/Ar du granite peralcalin du
929 lac Brisson, Labrador central, Nouveau-Québec. *Can J Earth Sci* 26:328–332
- 930 Poitrasson F, Duthou J-L, Pin C (1995) The relationship between petrology and Nd isotopes as evidence for
931 contrasting anorogenic granite genesis: example of the Corsican Province (SE France). *J Petrol*
932 36:1251–1274
- 933 Poitrasson F, Paquette J-L, Montel J-M, et al (1998) Importance of late-magmatic and hydrothermal fluids on the
934 Sm–Nd isotope mineral systematics of hypersolvus granites. *Chem Geol* 146:187–203
- 935 Rakotovo S, Rakotondrazafy R, Beziat D, et al (2009) Pétrologie du complexe alcalin cénozoïque
936 d’Ambohimirahavavy, presque île d’Ampasindava, nord-ouest de Madagascar. *Mada-Géo* 13:2–19
- 937 Ranløv J, Dymek RF (1991) Compositional zoning in hydrothermal aegirine from fenites in the Proterozoic
938 Gardar Province, South Greenland. *Eur J Mineral* 837–854. <https://doi.org/10.1127/ejm/3/5/0837>

- 939 Roelofsen JN (1997) The primary and secondary mafic silicates of two alkaline anorogenic complexes: Strange
940 Lake (Quebec-Labrador) and Amba Dongar (Gujarat, India). PhD Thesis, McGill University Libraries
- 941 Rønso JG, Pedersen AK, Engell J (1977) Titan-aegirine from early Tertiary ash layers in northern Denmark.
942 *Lithos* 10:193–204
- 943 Salvi S, Williams-Jones A (1995) Zirconosilicate phase relations in the Strange Lake (Lac Brisson) pluton,
944 Quebec-Labrador, Canada: *American Mineralogist*. *Am Mineral* 80:1031–1040.
945 <https://doi.org/10.2138/am-1995-9-1019>
- 946 Salvi S, Williams-Jones AE (1990) The role of hydrothermal processes in the granite-hosted Zr, Y, REE deposit
947 at Strange Lake, Quebec/Labrador: evidence from fluid inclusions. *Geochim Cosmochim Acta*
948 54:2403–2418
- 949 Salvi S, Williams-Jones AE (2006) Alteration, HFSE mineralisation and hydrocarbon formation in peralkaline
950 igneous systems: Insights from the Strange Lake Pluton, Canada. *Lithos* 91:19–34
- 951 Salvi S, Williams-Jones AE (1996) The role of hydrothermal processes in concentrating high-field strength
952 elements in the Strange Lake peralkaline complex, northeastern Canada. *Geochim Cosmochim Acta*
953 60:1917–1932
- 954 Salvi S, Williams-Jones AE (1997) Fischer-Tropsch synthesis of hydrocarbons during sub-solidus alteration of
955 the Strange Lake peralkaline granite, Quebec/Labrador, Canada. *Geochim Cosmochim Acta* 61:83–99
- 956 Sanematsu K, Kon Y, Imai A, et al (2013) Geochemical and mineralogical characteristics of ion-adsorption type
957 REE mineralization in Phuket, Thailand. *Miner Deposita* 48:437–451. [https://doi.org/10.1007/s00126-](https://doi.org/10.1007/s00126-011-0380-5)
958 [011-0380-5](https://doi.org/10.1007/s00126-011-0380-5)
- 959 Schmitt AK, Trumbull RB, Dulski P, Emmermann R (2002) Zr-Nb-REE mineralization in peralkaline granites
960 from the Amis Complex, Brandberg (Namibia): evidence for magmatic pre-enrichment from melt
961 inclusions. *Econ Geol* 97:399–413
- 962 Shannon RD (1976) Revised effective ionic radii and systematic studies of interatomic distances in halides and
963 chalcogenides. *Acta Crystallogr* 32:751–767
- 964 Sheard ER, Williams-Jones AE, Heiligmann M, et al (2012) Controls on the Concentration of Zirconium,
965 Niobium, and the Rare Earth Elements in the Thor Lake Rare Metal Deposit, Northwest Territories,
966 Canada. *Econ Geol* 107:81–104. <https://doi.org/10.2113/econgeo.107.1.81>
- 967 Shearer CK, Larsen LM (1994) Sector-zoned aegirine from the Ilimaussaq alkaline intrusion, South Greenland:
968 Implications for trace-element behavior in pyroxene. *Am Mineral* 79:340–352
- 969 Siegel K, Williams-Jones AE, Stevenson R (2017a) A Nd-and O-isotope study of the REE-rich peralkaline
970 Strange Lake granite: implications for Mesoproterozoic A-type magmatism in the Core Zone (NE-
971 Canada). *Contrib Mineral Petrol* 172:54
- 972 Siegel K, Williams-Jones AE, van Hinsberg VJ (2017b) The amphiboles of the REE-rich A-type peralkaline
973 Strange Lake pluton–fingerprints of magma evolution. *Lithos* 288:156–174
- 974 Smith MP (2007) Metasomatic silicate chemistry at the Bayan Obo Fe–REE–Nb deposit, Inner Mongolia, China:
975 contrasting chemistry and evolution of fenitising and mineralising fluids. *Lithos* 93:126–148
- 976 Smith MP, Henderson P, Jeffries TER, et al (2004) The rare earth elements and uranium in garnets from the
977 Beinn an Dubhaich Aureole, Skye, Scotland, UK: constraints on processes in a dynamic hydrothermal
978 system. *J Petrol* 45:457–484
- 979 Strong DF (1969) Formation of the hour-glass structure in augite. *Mineral Mag* 37:472–479
- 980 Sun S-S, McDonough W (1989) Chemical and isotopic systematics of oceanic basalts: implications for mantle
981 composition and processes. *Geol Soc Lond Spec Publ* 42:313–345

- 982 Thomas RJ, De Waele B, Schofield DI, et al (2009) Geological evolution of the Neoproterozoic Bemarivo Belt,
983 northern Madagascar. *Precambrian Res* 172:279–300. <https://doi.org/10.1016/j.precamres.2009.04.008>
- 984 Trail D, Bruce Watson E, Tailby ND (2012) Ce and Eu anomalies in zircon as proxies for the oxidation state of
985 magmas. *Geochim Cosmochim Acta* 97:70–87. <https://doi.org/10.1016/j.gca.2012.08.032>
- 986 U. S. Geological Survey (2019) Rare Earths Statistics and Information. In: *Miner. Commod. Summ.*
987 <https://www.usgs.gov/centers/nmic/rare-earths-statistics-and-information>. Accessed 28 Aug 2019
- 988 Ubide T, McKenna CA, Chew DM, Kamber BS (2015) High-resolution LA-ICP-MS trace element mapping of
989 igneous minerals: In search of magma histories. *Chem Geol* 409:157–168.
990 <https://doi.org/10.1016/j.chemgeo.2015.05.020>
- 991 Ubide T, Mollo S, Zhao J, et al (2019) Sector-zoned clinopyroxene as a recorder of magma history, eruption
992 triggers, and ascent rates. *Geochim Cosmochim Acta* 251:265–283.
993 <https://doi.org/10.1016/j.gca.2019.02.021>
- 994 Vasyukova O, Williams-Jones A (2020) Partial melting, fractional crystallisation, liquid immiscibility and
995 hydrothermal mobilisation—A 'Recipe' for the formation of economic A-Type granite-hosted HFSE
996 deposits. *Lithos* 356:105300
- 997 Vasyukova O, Williams-Jones AE (2014) Fluoride–silicate melt immiscibility and its role in REE ore formation:
998 Evidence from the Strange Lake rare metal deposit, Québec-Labrador, Canada. *Geochim Cosmochim*
999 *Acta* 139:110–130
- 1000 Vasyukova OV, Williams-Jones AE (2019) Closed system fluid-mineral-mediated trace element behaviour in
1001 peralkaline rare metal pegmatites: Evidence from Strange Lake. *Chem Geol* 505:86–99
- 1002 Vasyukova OV, Williams-Jones AE, Blamey NJF (2016) Fluid evolution in the Strange Lake granitic pluton,
1003 Canada: Implications for HFSE mobilisation. *Chem Geol* 444:83–100
- 1004 Veksler IV, Dorfman AM, Dulski P, et al (2012) Partitioning of elements between silicate melt and immiscible
1005 fluoride, chloride, carbonate, phosphate and sulfate melts, with implications to the origin of
1006 natrocarbonatite. *Geochim Cosmochim Acta* 79:20–40. <https://doi.org/10.1016/j.gca.2011.11.035>
- 1007 Wang Q, Deng J, Liu X, et al (2010) Discovery of the REE minerals and its geological significance in the
1008 Quyang bauxite deposit, West Guangxi, China. *J Asian Earth Sci* 39:701–712.
1009 <https://doi.org/10.1016/j.jseas.2010.05.005>
- 1010 William-Jones AE, Migdisov AA, Samson IM (2012) Hydrothermal mobilisation of the Rare Earth Elements—a
1011 Tale of " Ceria" and " Yttria. *Elements* 8:355–360
- 1012 Xu C, Kynický J, Smith MP, et al (2017) Origin of heavy rare earth mineralization in South China. *Nat Commun*
1013 8:14598
- 1014 Yang X-M, Yang X-Y, Zheng Y-F, Le Bas MJ (2003) A rare earth element-rich carbonatite dyke at Bayan Obo,
1015 Inner Mongolia, North China. *Mineral Petrol* 78:93–110
- 1016 Zaitsev AN, Terry Williams C, Jeffries TE, et al (2014) Rare earth elements in phoscorites and carbonatites of
1017 the Devonian Kola Alkaline Province, Russia: Examples from Kovdor, Khibina, Vuoriyarvi and Turiy
1018 Mys complexes. *Ore Geol Rev* 61:204–225. <https://doi.org/10.1016/j.oregeorev.2014.02.002>
- 1019
- 1020
- 1021 **Tables caption**

1022

1023 **Table 1** Mean values for the major and trace element composition, obtained by microprobe and LA-ICPMS
1024 respectively, of amphiboles from pegmatites and granites from the six complexes. Abbreviations: no.: number of
1025 replicates; F-arf: fluoro-arfvedsonite; F-f-f-lea: ferro-ferri-fluoro-leakeite; F-f-kato: ferro-ferri-katophorite; b.d.l.:
1026 below detection limit; Ambo: Ambohimirahavavy; KB: Khan bogd; M: Manongarivo; SL: Strange Lake

1027
1028 **Table 2** Mean values (number of analysis given in bold) for the major and trace element composition, obtained
1029 by microprobe and LA-ICPMS respectively, of aegirine from pegmatites and granites from six complexes
1030 worldwide in both pegmatites and granites. Granites only comprise type-II aegirine. T I, T II: aegirine type-I, II.
1031 Abbreviations: no.: number of replicates; b.d.l.: below detection limit; Ambo: Ambohimirahavavy; KB: Khan
1032 bogd; M: Manongarivo; SL: Strange Lake

1033
1034 **Table 3** Mean composition of cores and rims of type-I aegirine from 5 complexes. Abbreviations: no.: number of
1035 replicates; b.d.l.: below detection limit; Ambo: Ambohimirahavavy; KB: Khan bogd; M: Manongarivo

1036

1037 **Figures caption**

1038
1039 **Fig. 1** A logarithmic diagram plotting chondrite-normalized (Sun and McDonough 1989) values of whole-rock
1040 Yb/La vs Yb contents for different alkaline complexes worldwide. Five groups are distinguished: alkaline
1041 granites, alkaline pegmatites, carbonatites, nepheline syenites, and ion-adsorption deposits. Data are from this
1042 study plus from Estrade et al. (2014b), Boily and Williams-Jones (1994), Estrade (2014), Kynicki et al. (2011),
1043 Poitrasson et al. (1995), Vasyukova and Williams-Jones (2014), Schmitt et al. (2002), Moore et al. (2015), Yang
1044 et al. (2003), Xu et al. (2017), Liu et al. (2015), Zaitsev et al. (2014), Kogarko et al. (2002), Li et al. (2010),
1045 Sørensen et al. (1987), Hatch (2015), Sanematsu et al. (2013), Ishihara et al. (2008), Wang et al. (2010), and
1046 Chengyu et al. (1990)

1047
1048 **Fig. 2** Map localizing the six complexes studied in this paper. The geodynamic context and ages are given
1049 below their names in the rectangular boxes

1050

1051 **Fig. 3** Photographs of outcrop or hand samples of pegmatites from the six complexes. Most display a well-
1052 marked layering defined by mineralogy and textural variations

1053
1054 **Fig. 4** **a** Altered astrophyllite from Amis, **b** REE-bearing pseudomorph (Manongarivo), **c** Zircon-quartz
1055 pseudomorph (Evisa), **d** Elpidite (Khan Bogd), altered to armstrongite and zircon in its center, **e** Arfvedsonite
1056 replaced by type-II aegirine (Evisa), **f** A type-I aegirine showing core to rim zoning (Ambohimirahavavy), **g**
1057 Two tiny fluid inclusions in the rim of a type-I crystal of aegirine (Khan Bogd), **h** Mineral inclusions contained
1058 within the rim of a type-I aegirine (Ambohimirahavavy) that are of the same nature than minerals in REE-
1059 bearing pseudomorph, **i** A single crystal of type-II aegirine (Strange Lake), **j** Zoned amphibole, from katophorite
1060 in the core to arfvedsonite in the rims (Evisa), **k** A type-I aegirine showing core to rim zoning with zone B (Khan
1061 Bogd), **l** Zoned amphibole, from arfvedsonite in the core to leakeite in the rims (Evisa). Photographs **a, c, e, f, g,**
1062 **i** and **k** were taken with an optical microscope; photographs **b, h, j** and **l** with SEM EDS; and **d** with optical
1063 cathodoluminescence. pseudom: pseudomorph; zrn: zircon; aeg: aegirine; amph: amphiboles; qtz: quartz; afs:
1064 alkali feldspar; bsn: bastnäsite-(Ce); arf: arfvedsonite; ox: Ti- and Fe-oxides; calh: calciophilairite; CKZ:
1065 unidentified Ca- and K-bearing zirconosilicates; CMZ: unidentified Ca- and Mn-bearing zirconosilicates;
1066 NbYsil: unidentified Nb- and Y-bearing silicate; arm: armstrongite; elp: elpidite; astr: astrophyllite

1067
1068 **Fig. 5** Chemical composition of amphiboles. **a, b, c** Ternary diagrams representing amphibole poles for the **a**
1069 Evisa and Manongarivo complexes; **b** Ambohimirahavavy and Amis complexes; **c** Khan Bogd and Strange Lake
1070 complexes. Poles are plotted as 10 Mg and 10 Ca for a better visualization of the dataset. **d** Boxplots showing the
1071 trace-element composition of amphiboles from the different complexes. Thick black line represents the median,
1072 upper and lower boxplot limits the first and third quartile respectively, upper and lower dashed lines are the
1073 maximum and minimum values respectively, and the thin black line is the detection limit. Areas are shaded to
1074 distinguish data for each complex M: Manongarivo; Amb: Ambohimirahavavy; SL: Strange Lake; KB: Khan
1075 Bogd

1076
1077 **Fig. 6** Microprobe and LA-ICPMS maps on a type-I aegirine crystal at Ambohimirahavavy. Visible zonations
1078 were also found in the other complexes (see Supplementary material). 3 zones are distinguished: the core A, and
1079 the sector-zoned rims Cand D. Microprobe maps are in wt%, and LA-ICPMS maps are in ppm. Limits of

1080 aegirine on LA-ICPMS maps are blurry because the signal from the crystal and the matrix mix and do not reflect
1081 an actual concentration

1082

1083 **Fig. 7** Chemical composition of type-I and type-II aegirine crystals. Type-I aegirine is split between core and
1084 rim. Core and rim analyses are identified for Type-I aegirine. **a, b, c** are for aegirine, (Ti, Zr)-aegirine, and
1085 clinoferrosilite; when figures; **d, e, f** are for aegirine + (Ti, Zr)-aegirine, hedenbergite, and clinoferrosilite. **a, d**
1086 complexes Evisa and Manongarivo; **b, e** complexes Ambohimirahavavy and Amis; **c, f** Khan Bogd and Strange
1087 Lake; **g** Box diagrams comparing the trace element contents of aegirine from the different complexes. Thick
1088 black line represents the median, upper and lower boxplot limits the first and third quartile respectively, upper
1089 and lower dashed lines are the maximum and minimum values respectively, and the thin black line is the
1090 detection limit. Colours are keyed to the legend given in **a-f**. Areas are shaded to distinguish data for each
1091 complex

1092

1093 **Fig. 8** Logarithmic diagrams plotting chondrite-normalized REE composition obtained by LA-ICP-MS for
1094 amphiboles (normalization from Sun and McDonough, 1989) for all six complexes

1095

1096 **Fig. 9** Logarithmic diagrams plotting chondrite-normalized REE composition obtained by LA-ICPMS for
1097 aegirine (normalization from Sun and McDonough, 1989) for all six complexes. Large spectra presents all LA-
1098 ICP-MS analyses for type-I and type-II aegirine, whereas small spectra on the side show an example of analyses
1099 performed on a single type-I crystal

1100

1101 **Fig. 10** Diagram plotting REE concentration obtained by LA-ICPMS in the core and rim of type-I pyroxene in 5
1102 complexes. The typical analytical error is provided by the cross on the top right corner and is similar for all
1103 provided analyses

1104

1105 **Fig. 11** Histograms plotting the difference of REE concentration between the core and the rims of type-I
1106 aegirine, and thereby REE fractionation from core to rim. Negative values stand for a higher REE concentration

1107 in the core, and positive ones for a higher concentration in the rims. The rim enrichment in Khan Bogd is an
1108 artifact. Calculated error is shown by black lines at the end of the histogram bars

1109

1110 **Fig. 12** A schematic illustration of a model for aegirine and amphiboles formation. The arrows signify transfer of
1111 elements (in the boxes) to the different minerals from the melt or fluid (light blue), the line thickness is
1112 proportional to the amount of transfer, and a dashed line indicates a possible transfer. Ligands in the fluids are
1113 also shown. During the early magmatic stage, the competition for REE, Zr, Hf, Zr and Sn is low to moderate
1114 (depending on the co-presence or not of amphibole, pyroxene and complex zirconosilicate) and allows a relative
1115 enrichment in these elements in type-I aegirine and, mostly for REE, in amphibole. During the hydrothermal
1116 stage, the competition for these elements is stronger as it involves zircon and REE-bearing minerals;
1117 consequently, type-I aegirine rims are globally depleted. Fluids composition leads to a different mobilization of
1118 light and heavy REE, originating REE fractionation. Meanwhile, hydrothermal fluids replace amphiboles by
1119 type-II secondary aegirine and Fe-Ti-oxides

1120

1121 **Electronic Supplementary Material**

1122 **Online Resource 1** Text and maps detailing the geological background of all six studied complexes

1123

1124 **Online Resource 2** Table of standards used for calibration of EPMA and associated detection limits.

1125 Abbreviation: n.a.: not analyzed

1126

1127 **Online Resource 3** Table of detection limits for in situ LA-ICPMS measurements

1128

1129 **Online Resource 4** Microprobe maps on a type-I aegirine crystal at Amis. 3 zones are distinguished: A, the core
1130 rich in Ca, Zr, Sn, Hf and poor in Na, Fe; C, sector zoning rich in Ti, Ca; and D, sector zoning rich in Fe. The
1131 thick line represents limits of the map

1132

- 1133 **Online Resource 5** Microprobe maps on a type-I aegirine crystal at Evisa. 3 zones are distinguished: A, the
1134 core rich in Ca, Zr, Sn, Hf and poor in Na, Fe; C, sector zoning rich in Ti, Ca; and D, sector zoning rich in Fe.
1135 The thick line represents limits of the map
- 1136
- 1137 **Online Resource 6** Microprobe maps on a type-I aegirine crystal at Khan Bogd. 4 zones are distinguished: A,
1138 the core rich in Ca, Zr, Sn, Hf and poor in Na, Fe; B; C, sector zoning rich in Ti, Ca; and D, sector zoning rich in
1139 Fe
- 1140
- 1141 **Online Resource 7** Microprobe maps on a type-I aegirine crystal at Manongarivo. 3 zones are distinguished: A,
1142 the core rich in Ca, Zr, Sn, Hf and poor in Na, Fe; C, sector zoning rich in Ti, Ca; and D, sector zoning rich in Fe
- 1143
- 1144 **Online Resource 8** Microprobe maps on a type-II aegirine crystal at Strange Lake. No core-to-rim zoning is
1145 observed, but an oscillatory zoning occurs for most elements
- 1146